nature communications

Article

https://doi.org/10.1038/s41467-024-54868-w

A bioinspired sulfur–Fe–heme nanozyme with selective peroxidase-like activity for enhanced tumor chemotherapy

Received: 4 March 2024

Accepted: 22 November 2024

Published online: 05 December 2024

Check for updates

Shuaibing Zhang[1,2,7], Xuejiao J. Gao[3,7], Yuanjie Ma[3], Kexu Song[1], Mengyue Ge[1], Saiyu Ma[1], Lirong Zhang[4], Ye Yuan[1], Wei Jiang[1], Zhenzhen Wu[5], Lizeng Gao[1,2,6] ✉, Xiyun Yan[1,2,6] ✉ & Bing Jiang[1,2,4] ✉

Iron-based nanozymes, recognized for their biocompatibility and peroxidase-like activities, hold promise as catalysts in tumor therapy. However, their concurrent catalase-like activity undermines therapeutic efficacy by converting hydrogen peroxide in tumor tissues into oxygen, thus diminishing hydroxyl radical production. Addressing this challenge, this study introduces the hemin–cysteine–Fe (HCFe) nanozyme, which exhibits exclusive peroxidase-like activity. Constructed through a supramolecular assembly approach involving Fmoc-L-cysteine, heme, and Fe^{2+} coordination, HCFe distinctly incorporates heme and [Fe–S] within its active center. Sulfur coordination to the central Fe atom of Hemin is crucial in modulating the catalytic preference of the HCFe nanozyme towards peroxidase-like activity. This unique mechanism distinguishes HCFe from other bifunctional iron-based nanozymes, enhancing its catalytic selectivity even beyond that of natural peroxidases. This selective activity allows HCFe to significantly elevate ROS production and exert cytotoxic effects, especially against cisplatin-resistant esophageal squamous cell carcinoma (ESCC) cells and their xenografts in female mice when combined with cisplatin. These findings underscore HCFe's potential as a crucial component in multimodal cancer therapy, notably in augmenting chemotherapy efficacy.

Nanozymes, emerging as a specialized category of nanomaterials, are noted for their enzymatic properties, synergizing the merits of traditional enzymes and chemical catalysts[1,2]. They are renowned for their ability to catalyze enzyme–substrate reactions under mild conditions, attributed to their robust catalytic activity, stability, cost-effectiveness, ease of modification, and potential for large-scale production[3]. These attributes propel nanozymes as formidable alternatives to natural enzymes in diverse applications including disease diagnosis and treatment[4,5], analytical chemistry[6–8], biosensing[9–11], and environmental remediation[12,13]. However, nanozymes are often critiqued for their diminished selectivity compared to natural enzymes, which boast of high specificity for substrates and reaction pathways. Recent research has aimed to overcome this challenge by enhancing their specificity. Li et al. developed an oxidase-like MOF-818 nanozyme that mimics

[1]Nanozyme Laboratory in Zhongyuan, School of Basic Medical Sciences, Zhengzhou University, Zhengzhou, China. [2]Nanozyme Laboratory in Zhongyuan, Henan Academy of Innovations in Medical Science, Zhengzhou, China. [3]College of Chemistry and Chemical Engineering, Jiangxi Normal University, Nanchang, China. [4]Department of Pharmacology, School of Basic Medical Sciences, Zhengzhou University, Zhengzhou, China. [5]Key Laboratory of Epigenetic Regulation and Intervention, Institute of Biophysics, Chinese Academy of Sciences, Beijing, China. [6]CAS Engineering Laboratory for Nanozyme, Key Laboratory of Biomacromolecules, Institute of Biophysics, Chinese Academy of Sciences, Beijing, China. [7]These authors contributed equally: Shuaibing Zhang, Xuejiao J. Gao. ✉e-mail: gaolizeng@ibp.ac.cn; yanxy@ibp.ac.cn; jiangbing@zzu.edu.cn

natural catechol oxidase, achieving high specificity for catechol oxidation[14]. Wang et al. regulated the peroxidase-like specificity of molybdenum single-atom nanozymes (MoSA-Nx-C) through coordination number adjustments[15]. Xu et al. introduced an "electron lock" strategy in iron-doped carbon dot nanozymes to control catalytic selectivity by manipulating electron transfer[16]. These advancements showcase promising approaches to fine-tune nanozyme selectivity, broadening their potential applications in complex systems.

Iron-based nanozymes, characterized by their excellent biocompatibility and peroxidase-like (POD) activity, are particularly potent in catalyzing the conversion of H_2O_2 to hydroxyl radicals in the tumor microenvironment, opening frontiers in tumor catalytic therapy[17,18]. Contrary to the inherent high catalytic selectivity of natural PODs, these nanozymes present pH-dependent bifunctional enzymatic activities encompassing both POD and catalase functions[19,20]. In the presence of hydrogen peroxide as a substrate, iron-based nanozymes manifest diverse catalytic routes. The CAT activity specifically undermines therapeutic efficacy by converting available H_2O_2 in tumor tissues to oxygen, reducing hydroxyl radical formation. This complexity necessitates refined strategies to harness the full potential of iron-based nanozymes. The quest for iron-based nanozymes with a singular POD activity is driven by the imperative to enhance the effectiveness of nanozyme-based tumor catalytic therapy. The elimination of competing CAT activity can potentially unshackle the full therapeutic potential of these nanozymes.

Previous analyses of the active center architectures of natural PODs and catalases have revealed that both enzymes inherently contain the prosthetic group hemin[21–24]. As a crucial prosthetic group in natural oxidoreductases, hemin features a central iron atom (Fe) coordinated with four nitrogen atoms ($Fe–N_4$), forming its basic coordination environment. This environment plays a vital role in the redox functionality of enzymes. However, we noted that the contributory amino acid residues in the catalytic centers of natural PODs and catalases differ significantly. This led us to hypothesize that manipulating the coordination environment of hemin could potentially modulate the catalytic selectivity and specificity of hemin-based enzymes. Additionally, Iron–sulfur (Fe–S) structures also play a crucial role in natural oxidoreductases[25–27]. These structures, comprising iron and sulfur atoms, form the active centers and participate in substrate binding and transformation. Fe–S structures are key inorganic cofactors that facilitate the catalytic activity of various enzymes, including dehydrogenases, hydrogenases, and certain monooxygenases. They catalyze a wide array of chemical reactions, such as the breaking of carbon-hydrogen bonds and various oxidation reactions, primarily by participating in redox reactions and facilitating electron transfer. The versatility of the iron atoms in iron–sulfur structures to switch between different oxidation states enhances their effectiveness as electron transfer mediators, and further facilitates the oxidation of substrates. The crucial roles of hemin and Fe–S structures in redox reactions suggest an approach: combining hemin and Fe–S structures to create an active center, potentially enhancing the catalytic selectivity and specificity of hemin-based nanozymes towards POD-like activity.

In this work, we develop a hemin–cysteine–Fe (HCFe) nanozyme that exhibits catalytic selectivity and exclusive POD-like activity. Our approach involved integrating sulfhydryl groups to coordinate with the iron atom in hemin, forming an ancatalytic center. Using a supramolecular assembly process with Fmoc-L-cysteine, heme, and Fe^{2+} coordination, we synthesized an HCFe nanozyme. The HCFe nanozyme demonstrated exclusive POD-like activity in mildly acidic conditions, attributed to the electron-donating influence of sulfur in its coordination with the iron atom in hemin. The absence of catalase-like activity amplifies HCFe's potential in ROS-mediated tumor therapy. Our study further explores the synergy of HCFe with cisplatin (CDDP) to overcome CDDP-resistance in esophageal squamous cell carcinoma (ESCC), offering insights into molecular mechanisms, including enhanced ROS generation, reduced drug efflux, and cellular glutathione depletion. These findings highlight HCFe's potential as a key component in multimodal cancer therapies, especially in improving the efficacy of chemotherapy in resistant cancers (Fig. 1).

Results and discussion

Creation of HCFe nanozyme by the integration of heme and Fe–S structures

To synthesize a nanozyme that incorporates heme and Fe–S at its active site, we employed a supramolecular assembly approach. This approach involved fabricating biomimetic self-assembled iron-based nanozymes, capitalizing on the π-π stacking interactions between Fmoc-modified L-cysteine and heme. Additionally, Fe^{2+} was introduced to coordinate with carboxyl groups, ensuring nanostructure stability (Fig. 2a). Consequently, the HCFe nanozyme was successfully synthesized. To elucidate its assembly process and quantify the interactions among key structural units, density functional theory (DFT) calculations were performed. As depicted in Fig. 2b, the initial step involves the binding of Fmoc-L-cysteine and hemin through coordination interactions to form the hemin–Fmoc-L-cysteine complex, exhibiting a binding energy of −52.6 kcal/mol. This is followed by the coordination of Fe^{2+} with two carboxylate groups, resulting in a stabilized tetracoordinated structure with a binding energy of −402.3 kcal/mol. This significantly strong interaction force implies that the incorporation of Fe^{2+} facilitates the assembly of HCFe nanozymes, thereby enhancing the stability of the nanostructures. Ultimately, two Fe^{2+}–hemin–Fmoc-L-cysteine monomers are combined to form HCFe nanozymes through π-π stacking interactions, with an interaction energy of −9.3 kcal/mol. The existence of two conjugated fragments, the coplanar conjugation in Fmoc-L-cysteine and the porphyrin ring, enables various stacking modes. Here, we demonstrate a specific mode where the stacked portion is the coplanar conjugated ring within Fmoc-L-cysteine. The interaction energy of −9.3 kcal/mol corroborates the assembly of Fe^{2+}–hemin–Fmoc-L-cysteine monomers into nanoparticles through weak π-π interactions. To explore the unique properties of the HCFe nanozyme, a comprehensive array of biomimetic iron-based nanozymes was generated using the remaining 19 distinct Fmoc-L-amino acids, as demonstrated in Fig. 2c. Transmission electron microscopy (TEM) imaging was employed to characterize the synthesis of 20 distinct nanozymes. These images revealed that each nanozyme exhibited nanostructured forms; notably, some displayed cross-linked network structures, while others presented monodispersed spherical morphologies. Dynamic light scattering (DLS) measurements indicated that these nanozymes were monodispersed with homogeneously hydrated particle sizes ranging between 40 nm and 100 nm, as shown in Supplementary Fig. S1. Additionally, the zeta potential measurements of these nanozymes consistently demonstrated negative values (Fig. S2).

Subsequently, the nanozymes were assessed for POD-like activities at pH 4.5 and CAT-like activities at pH 7.4. The experimental outcomes revealed that all these nanozymes exhibited the capability to facilitate the oxidation of TMB by H_2O_2 at pH 4.5, corroborating their POD-like activity (Figs. 2d and S3a). In contrast, a notable deviation was observed in their behavior at pH 7.4; the HCFe nanozyme uniquely lacked the ability to expedite the decomposition of H_2O_2 to oxygen, denoting an absence of CAT-like activity, a characteristic unshared by the 19 other variants and hemin (Figs. 2d and S3b). These 19 variants and hemin showed both POD and CAT activities, indicating that the unique lack of CAT-like activity in HCFe stemmed from the coordination of cysteine. Significantly, natural horseradish peroxidase (HRP) showed a minor degree of catalase-like activity further illustrating the HCFe nanozyme's precise catalytic pathway selectivity and its exclusive POD performance (Figs. 2d and S4).

The distinctiveness of HCFe nanozymes in catalyzing the generation of hydroxyl radicals from H_2O_2, without its decomposition to

https://doi.org/10.1038/s41467-024-54868-w

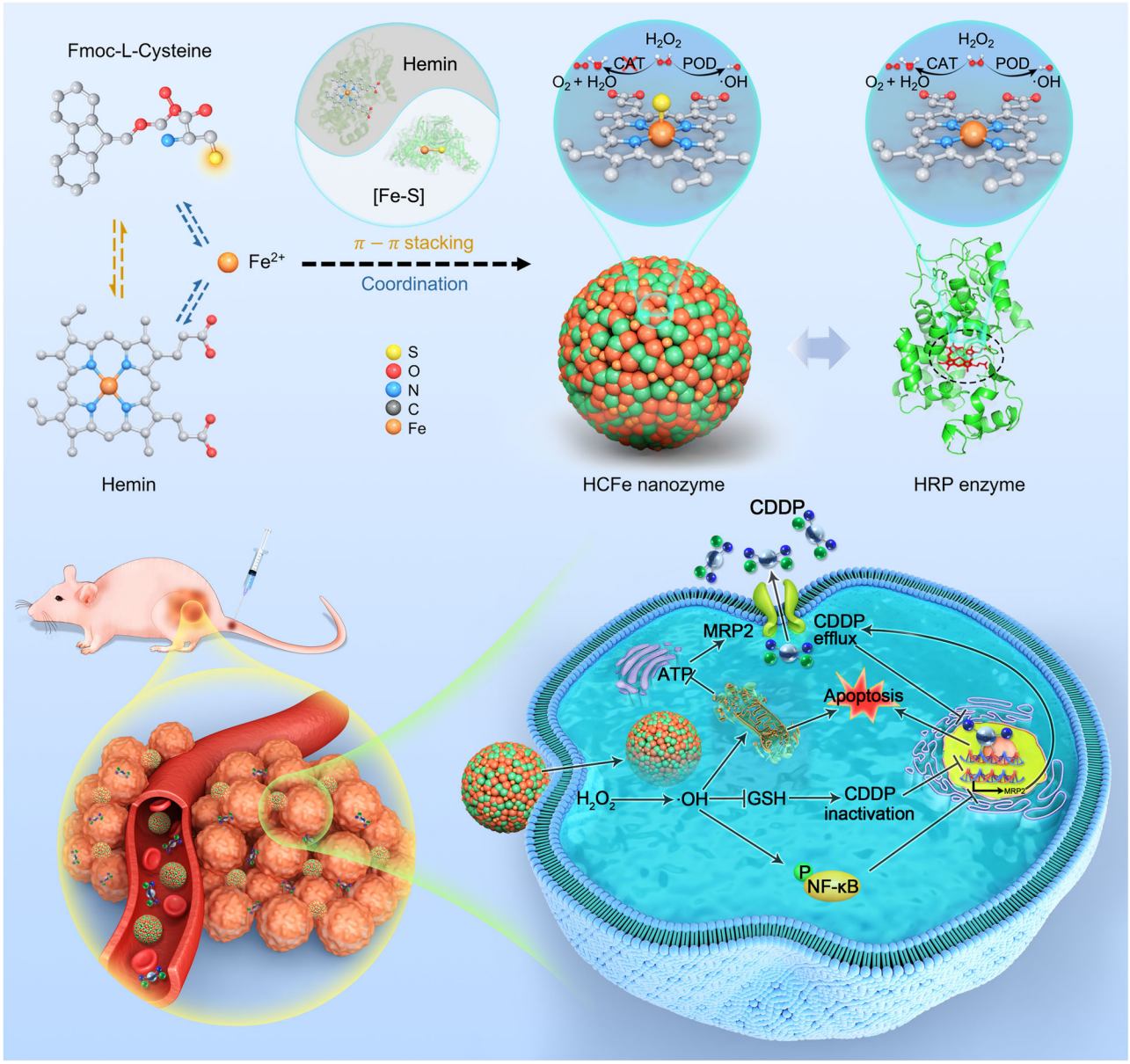

Fig. 1 | Schematic illustration of synthesis and screening of HCFe nanozyme and its applications in overcoming cisplatin resistance in esophageal squamous cell carcinoma (ESCC) chemotherapy. The HCFe nanozyme is synthesized using a supramolecular assembly approach that integrates Fmoc-L-cysteine, hemin, and Fe^{2+}. This process results in the formation of a catalytic center featuring the structural integration of [Fe–S] and hemin, with sulfur coordination playing a critical role in selectively POD-like activity. The HCFe nanozyme overcomes cisplatin resistance by inducing excessive ROS, which suppresses CDDP efflux, depletes intracellular GSH, and enhances DNA damage and cell apoptosis, thereby restoring the chemotherapeutic sensitivity of resistant ESCC cells. Structural representations for horseradish peroxidase (7ATJ) and aldehyde oxidase (5Y6Q) were derived from publicly accessible Protein Data Bank (PDB) data, illustrating enzymes with hemin and [Fe–S] in their catalytic centers, respectively.

water and oxygen, necessitated a more nuanced evaluation. A comparative analysis of POD-like and catalase-like activities under identical pH conditions was conducted. Given the relevance of a mildly acidic milieu in the context of tumor catalytic therapy, a reassessment of the nanozymes' activities was executed at pH 6.5. The findings accentuated the specialized catalytic orientation of HCFe nanozyme, manifesting exclusive mono-POD activity in a mildly acidic milieu (Figs. 2d and S3c, d).

To thoroughly assess the CAT-like activity of the HCFe nanozyme, we monitored the absorbance of H_2O_2 under various pH conditions. The results demonstrated that the HCFe nanozyme did not significantly reduce H_2O_2 absorbance, indicating a lack of CAT-like activity across these pH settings (Fig. S5). Using a catalase assay kit, we evaluated the CAT-like activity of HCFe nanozyme, HHFe nanozyme, and HRP. The findings revealed that while HHFe nanozyme and HRP exhibited CAT-like activity, HCFe nanozyme did not (Fig. S6).

Additionally, we investigated both POD-like and CAT-like activities of 20 different nanozymes in deionized water. The results indicated that none of the nanozymes displayed POD-like activity in the pH-neutral environment of deionized water, suggesting that such activity is absent under these conditions. Interestingly, of all the nanozymes tested, only the HCFe nanozyme lacked CAT-like activity in deionized water, whereas the remaining 19 nanozymes demonstrated significant CAT-like activity, aligning with observations made at pH 6.5 and pH 7.4 (Fig. S7).

In summation, HCFe nanozymes exhibit a distinct characteristic marked by the exclusive POD-like activity, notably absent in the other 19 nanozyme variants and hemin that demonstrate both POD and CAT

https://doi.org/10.1038/s41467-024-54868-w

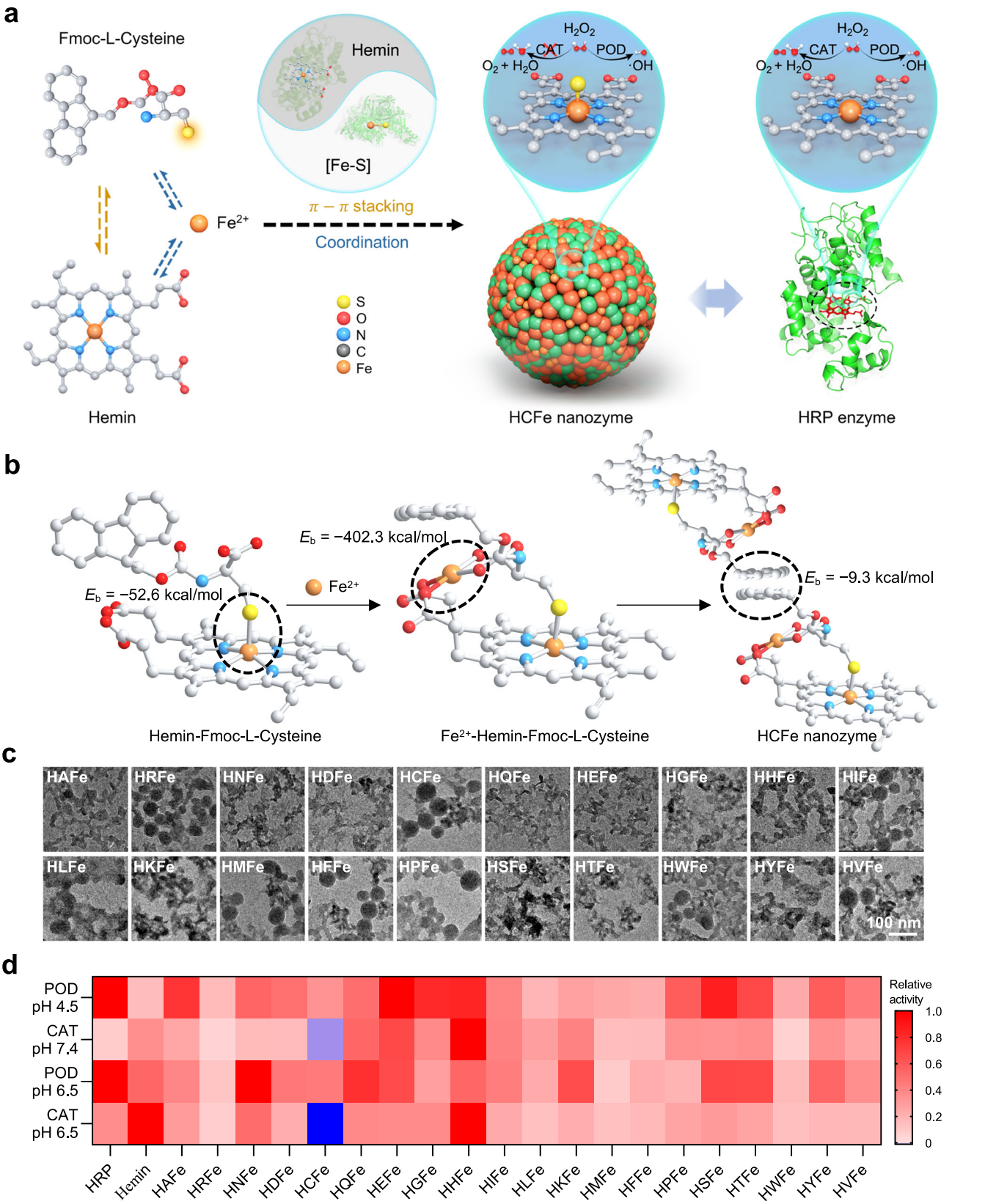

Fig. 2 | Construction of a biomimetic self-assembled iron-based nanozyme library and screening of iron-based mono-POD nanozyme. a Schematic diagram of the synthesis of biomimetic self-assembled iron-based nanozymes. **b** The assembly process of the HCFe nanozyme and the quantification of interactions among key structural units were determined through DFT calculations. E_b refers to the binding energy between two molecules and is calculated as the energy difference between the complex and the individual separated molecules. In the ball-and-stick models, the orange, yellow, blue, red, and gray–white balls represent the Fe, S, N, O, and C elements, respectively. **c** Representative TEM images of 20 biomimetic self-assembled iron-based nanozymes. **d** Heat map for comparison of the normalized reaction velocity of biomimetic self-assembled iron-based nanozymes. Data are presented as mean ± SD ($n = 3$ independent experiments). Source data are provided as a Source Data file.

activities. Remarkably, under conditions where hydrogen peroxide is the only substrate, the HCFe nanozyme does not catalyze its decomposition into water and oxygen. This unique property not only confirms HCFe nanozyme's superior catalytic selectivity compared to most catalysts but also highlights its advantage in preventing the unwanted production of oxygen—a side reaction commonly associated with natural HRP. This unique catalytic specificity warrants the categorization of HCFe as an iron-based mono-POD nanozyme.

Structural analysis of HCFe mono-POD nanozyme

The comprehensive examination of HCFe nanozyme was extended, unveiling intricate nuances of its structural and functional attributes. TEM images illustrated a well-defined spherical morphology of HCFe nanozyme (Fig. 3a). Energy dispersive spectroscopy (EDS) mappings affirmed a homogenous dispersion of C, N, O, S, and Fe elements across the entire spherical configuration (Fig. 3b, c). An aberration-corrected high-angle annular dark field scanning TEM (AC HAADF-STEM) analysis was conducted to provide direct observation of the atomic structure of the HCFe nanozyme. A distinctly bright dot indicated the atomic dispersion of single Fe atoms across the HCFe nanozyme structure (Fig. 3d). Organic element analysis was employed to quantify the composition of carbon (C), nitrogen (N), and sulfur (S), while inductively coupled plasma mass spectrometry (ICP-MS) was utilized for the assessment of iron (Fe) content within the HCFe nanozyme. The analyses revealed that C, N, S, and Fe constituted 55.60%, 6.28%, 5.50%, and 10.93% of the composition, respectively (Table S1). These findings provide evidence for the concurrent presence of N, S, and Fe within the structural composition of HCFe nanozymes. The dynamic light scattering (DLS) assessment depicted a particle size distribution of 63.19 ± 13.51 nm and a Zeta potential of −22.74 ± 8.148 mV for the HCFe nanozyme (Figs. S1 and S2).

The surface composition of the HCFe nanozyme was explored using X-ray photoelectron spectroscopy (XPS). Analysis revealed the presence of carbon (C 284.8 eV), nitrogen (N 398.48 eV), oxygen (O 531.71 eV), sulfur (S 164.13 eV), and iron (Fe 711.12 eV) (Fig. S8a). Detailed inspection of the high-resolution C1*s* spectra unveiled four distinct peaks corresponding to various functional groups: C=O (289.04 eV), C–O (287.13 eV), C–N (285.69), and C–C (284.82 eV) (Fig. S8b). Similarly, the N1*s* spectra were deconvoluted into three component peaks at 397.31 eV, 398.72 eV, and 400.11 eV, aligning with Fe–N, H–N, and C–N, respectively (Fig. S8c). This spectral data corroborates the retention of functional groups inherent to the hemin precursor on the HCFe nanozyme surface. Examination of the O1*s* spectra yielded peaks characteristic of Fe–O (530.6 eV), C–O (531.69 eV), and C=O (533.3 eV) (Fig. S8d), providing evidence for the specific coordination of iron with the carboxyl groups present in hemin or cysteine.

A comprehensive analysis of the Fe2*p* XPS spectra identified twelve distinct peaks ascribed to varied states and coordinations of iron and sulfur, which are Fe^{2+} $2p_{3/2}$ (708.3 eV), Fe^{2+} $2p_{1/2}$ (721.76 eV), Fe^{2+} $2p_{sat}$ (712.78 eV and 725.73 eV), Fe^{3+} $2p_{3/2}$ (710.52 eV), Fe^{3+} $2p_{1/2}$ (723.64 eV), Fe^{3+} $2p_{sat}$ (715.03 eV and 729.02 eV), Fe–S $2p_{3/2}$ (709.18 eV), Fe–S $2p_{1/2}$ (722.48 eV), Fe–N $2p_{3/2}$ (707.24), and Fe–N $2p_{1/2}$ (Fig. 3e). These data intimate the coexistence of iron in dual electronic states, fostering an environment conducive for enhanced POD-like activity. The elucidation of the Fe2*p* spectra accentuates the complex interplay between iron and sulfur, an assertion substantiated by the detailed S2*p* spectra. As delineated in Fig. 3f, the S2*p* spectra are demarcated by six distinct peaks, specifically Fe–S $2p_{3/2}$ (161.44 eV), Fe–S $2p_{1/2}$ (162.8 eV), S $2p_{3/2}$ (163.88 eV), S $2p_{1/2}$ (165.2 eV), S–O $2p_{3/2}$ (166.78 eV), and S–O $2p_{1/2}$ (168.64 eV). This array of peaks underscores the coordination of sulfur and iron, amplifying our understanding of its possible influence on the catalytic specificity exhibited by the HCFe nanozyme.

To elucidate the iron coordination environment and the interaction between Fe and S in the HCFe nanozyme, the Mössbauer spectrums of the HCFe nanozyme and hemin were detected. IS is an isomeric shift, which reflects the information of electrons in the nucleus, including electron density, valence state, chemical shift, etc. QS is a quadrupole split, which reflects the degree to which the nucleus deviates from the spherical symmetry, including the distortion, expansion, collapse, lattice, etc. As shown in Fig. 3g, h and Table S2, hemin has only one single peak (Singlet), its IS is 0.01 mm/s, but no QS, which indicates that hemin is a highly symmetrical planar structure. HCFe has a quadrupole Doublet, its IS is 0.37 mm/s, and QS is 0.78 mm/s, which indicates that the Fe in HCFe is in a three-dimensional structure that deviates from the spherical symmetry. This indicates that the $Fe–N_4$ square-planar structure of hemin within HCFe nanozymes has been altered to a three-dimensional structure. This alteration supports the formation of the $Fe–N_4S$ structure.

Additional insights into the HCFe nanozymes were gleaned through X-ray absorption fine structure spectroscopy (XAFS), illuminating the dispersion and coordination milieu of Fe elements. The X-ray absorption near edge structure (XANES) spectra, benchmarked against Fe_2O_3 references, unveil the Fe K-edge attributes of the HCFe nanozymes, as illustrated in Fig. 3i. Edge energy absorption (Eb) delineations suggest the Fe atoms are in specific oxidation states, with the pre-edge peak of HCFe markedly aligning with that of Fe_2O_3. In the Fourier-transformed realm (R space), extrapolations from the k^2-weighted EXAFS data (Fig. 3j) were adeptly maneuvered to yield quantitative EXAFS analyses. Structural parameters, encapsulated in Table S3, unveil a distinct Fe–N, and Fe–S coordination within HCFe nanozymes. The Fe atoms are proximally situated at 2.069 Å from the four N atoms (Fe–N) and at a 2.270 Å expanse from the one S atom (Fe–S). A conspicuous phase shift underpins the divergences between peak positions in R space and the fitting table. The congruence of fitting graphs with original data in both K and R spaces attests to the robustness and credibility of the fitting outcomes, as corroborated in Fig. S9. Figure 3k–o illustrates the wavelet transform (WT) of the EXAFS spectra. Fe_2O_3 displays intensity peaks at approximately 4.5 $Å^{-1}$ (Fig. 3l), attributable to the Fe–O coordination path. Hemin shows similar intensity peaks at around 4.5 $Å^{-1}$, which are ascribed to the Fe–N coordination path (Fig. 3m). In contrast, FeS_2 exhibits its intensity maxima at about 7.9 $Å^{-1}$, indicative of the Fe–S coordination path (Fig. 2n). The HCFe nanozyme, however, demonstrates intensity peaks at 5.5 $Å^{-1}$, distinctly shifted to the right compared to hemin, signifying the formation of Fe–S bonds along the axial direction of hemin within the HCFe nanozyme structure (Fig. 3o). Consequently, both WT and Fourier-transformed EXAFS (FTEXAFS) analyses substantiate the presence of Fe–N/O coordination and Fe–S bonds in the HCFe nanozyme.

We further conducted theoretical XANES simulations of the Fe–K edge using the full multi-scattering (FMS) approach within the framework of the Muffin-tin approximation for potential in real space[28,29]. The FeN_4S configuration was subjected to near-edge simulation calculations, and we compared the resulting data with experimental measurements. As shown in Fig. S10, the synchrotron radiation-based near-edge calculation results align well with the experimental data, thereby validating the rationality of the proposed FeN_4S configuration presented in HCFe nanozyme. We then conducted a detailed analysis of synchrotron radiation data. The valence state of Fe was accurately determined from the first-order derivative of the Fe K-edge XANES (Fig. S11a). The average oxidation states of Fe in HCFe and hemin were found to be +2.51 and +2.77, respectively (Fig. S11b). Further, the Fe K-Edge EXAFS and Mössbauer spectrum analyses suggest that the decrease in the average oxidation state of Fe in HCFe is attributable to strong electron transfer from the Fmoc-L-cysteine to the Fe atom, caused by bridging S on the $Fe–N_4$ plane structure of hemin (Fig. 3g, j). This supports the formation of the FeN_4S structure, which is consistent with the results of DFT calculations (Fig. 2b).

Additionally, we conducted X-ray absorption spectroscopy (XAS) tests to evaluate the structural stability of HCFe nanozymes before and

https://doi.org/10.1038/s41467-024-54868-w

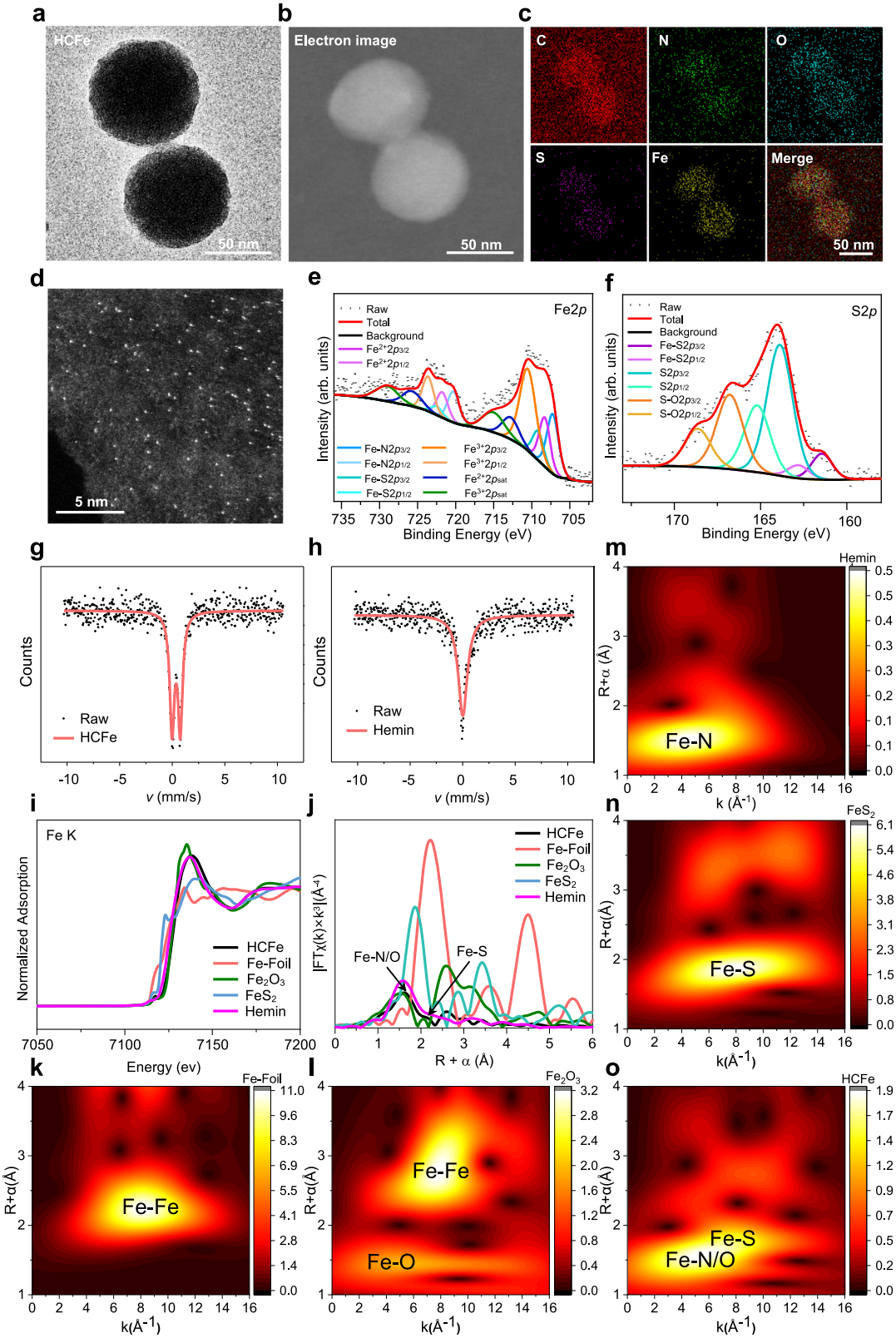

Fig. 3 | Structural characterization of HCFe iron-based mono-POD nanozyme. Representative TEM image (**a**), Electron image (**b**), and EDS element mapping (**c**) of HCFe nanozyme. Scale bar = 50 nm. **d** Representative AC HAADF-STEM image. Scale bar = 5 nm. **e** Fe2*p* XPS spectrum. **f** S2*p* XPS spectrum. Mössbauer spectrum fitting analysis of HCFe nanozyme (**g**) and hemin (**h**). **i** Normalized Fe K-edge XANES. **j** FTEXAFS spectra. WT images of the Fe K-edge from Fe-foil (**k**), Fe_2O_3 (**l**), hemin (**m**), FeS_2 (**n**) and HCFe nanozyme (**o**). Source data are provided as a Source Data file.

after the enzyme-like reaction. The Fe K-edge XANES analysis revealed no significant changes in the oxidation state of Fe atoms before and after the reaction (Fig. S12a). The Extended X-ray absorption fine structure (EXAFS) analysis of the electronic structure of the central Fe atom showed consistent results, with no significant shifts in the Fe–N/O bonds at 1.6 Å and Fe–S bonds at 2.2 Å (Fig. S12b, c). EXAFS fitting analysis confirmed the specific coordination mechanism of the central iron, demonstrating that the coordination numbers remained unchanged, as shown in Table S4. This underscores the robust structural stability of HCFe nanozymes' key units throughout the catalytic process.

Furthermore, we measured the Fe content in the supernatant after the POD-like activity assay using ICP-MS to monitor any potential Fe ion leakage. The results suggested negligible Fe ion leakage during the catalytic activity of HCFe nanozymes (Table S5). These findings further support the conclusion that HCFe nanozymes maintain excellent structural stability during the catalytic reaction process.

Characterization of the catalytic performance of HCFe mono-POD nanozyme

The investigative focus then transitioned to the enzymatic activity, where it was discerned that the isolated components of the HCFe nanozyme—hemin and Fe^{2+}, as well as the combined mixture of hemin, Fe^{2+}, and Fmoc-L-cysteine—demonstrated significant catalytic capabilities for the oxidation of the POD substrate TMB. However, their activities were lower than that of the complete HCFe nanozyme when compared at equivalent mass concentrations under either pH 4.5 or pH 6.5. This observation underscored that the exhibited enzymatic activity was attributed not to individual elements or the liberation of iron ions in the solution, but to the synergistic constitution of the composite structure. The HCFe nanozyme's composite structure facilitates a more effective integration of components, enhancing its POD-like activity (Fig. 4a, b).

Additionally, we assessed the CAT-like activity of the HCFe nanozyme, hemin, Fmoc-L-cysteine, Fe^{2+}, the supernatant of HCFe, and the mixture of hemin, Fmoc-L-cysteine, and Fe^{2+} at both pH 6.5 and pH 7.4. The results showed that while the hemin component within the HCFe nanozyme exhibited significant CAT activity at these pH levels, the HCFe nanozyme itself did not demonstrate any CAT activity (Fig. 4c, d). This observation supports the conclusion that the HCFe nanozyme modifies the coordination microenvironment of hemin, effectively eliminating its CAT-like activity and instead, displaying solely POD-like activity. It's worth noting that the mixture of hemin, and Fmoc-L-cysteine showed CAT activity similar to that of hemin alone (Fig. 4c, d). This suggests that the catalytic properties of the HCFe nanozyme arise from the composite structure of its components rather than from a simple mixture.

Furthermore, we evaluated the activity of HCFe nanozymes at various concentrations and subsequently calculated their specific activity. As demonstrated in Fig. S13, there is a linear relationship between the activity and the mass of the HCFe nanozyme. The specific activity of the HCFe nanozyme was determined to be 1.332 U/mg. The kinetic behavior of this nanozyme, when interacting with substrates TMB or H_2O_2, adhered to the Michaelis–Menten kinetics, underscoring the POD-like activity of HCFe (Fig. S14). As detailed in Table S6, we calculated the catalytic rate constant (K_{cat}) and the catalytic efficiency ($Kcat/K_m$) for reactions using TMB and H_2O_2 as substrates. These calculations were performed using the formula $K_{cat} = V_{max}/[E_t]$, where $[E_t]$ represents the total nanozyme concentration. These results indicate that the catalytic behavior of HCFe nanozyme conforms to the enzymatic characteristics.

A comparative analysis of the POD-like and CAT-like activities was conducted under conditions mimicking the tumor's acidic microenvironment (pH 6.5) and the normal physiological environment (pH 7.4). Data evidenced an absence of CAT-like activity and a pH 6.5-constrained manifestation of POD-like activity for the HCFe nanozyme (Fig. 4e, f). These observations intimate a pH-responsive activation state of the nanozyme, being inert at physiological pH and becoming enzymatically active in the acidic tumor milieu (Fig. 4g). Electron spin resonance (ESR) corroborated these findings, showcasing the capability of HCFe nanozyme to instigate ·OH production from H_2O_2 at pH 6.5, whilst remaining inactive at pH 7.4 (Fig. 4h). Such pH-dependent enzymatic behavior augments the biosafety profile of the HCFe nanozyme in tumor therapy. In the normal physiological context, its inert state ensures biocompatibility, whilst its activation within the acidic tumor microenvironment underpins its therapeutic efficacy via the generation of •OH to eradicate tumor cells.

To delineate the superior efficacy of HCFe nanozyme in tumor catalytic therapy, a comparative analysis was conducted with HHFe nanozyme serving as a reference. The latter, though exhibiting analogous POD-like activity to HCFe, possesses pronounced CAT-like activity as well (Fig. 4i). Electron spin resonance (ESR) was employed to quantify the •OH radicals produced from H_2O_2 catalyzed by both nanozymes at pH 6.5. The quantitative data affirmed that HCFe facilitated a greater yield of •OH radicals compared to HHFe at identical H_2O_2 concentrations (Fig. S15). Intracellular ROS levels, as quantified in EC109 cells, underscored a heightened ROS generation in cells treated with HCFe nanozymes relative to those exposed to HHFe counterparts (Fig. 4j). This distinction accentuates HCFe's superior efficacy in inducing ROS generation within tumor cells. Consistently, cytotoxicity assays revealed a marked reduction in cell viability in EC109 populations treated with HCFe, attesting to its potent cytotoxic impact relative to HHFe (Fig. 4k). Collectively, these insights unveil HCFe's enhanced proficiency in facilitating H_2O_2 catalysis to yield •OH radicals, engendering elevated ROS levels within tumor cells, thereby amplifying its cytotoxic effects relative to HHFe, which exhibits both POD and CAT activities (Fig. 4l).

An extended comparative analysis juxtaposed HCFe with other established iron-based nanozymes (including Fe_3O_4, hemin–Fe_3O_4, FeN_4C, and α-FeNC)[1,30] under the acidic tumor microenvironment (pH 6.5). HCFe emerged as the exclusive nanozyme showcasing singular POD-like activity and demonstrated superior efficacy in the oxidation of TMB by H_2O_2 (Fig. S16e, f). ESR analyses reiterated HCFe's enhanced capacity for •OH radical generation from H_2O_2 under analogous conditions (Fig. S16g). Interestingly, despite HCFe not showcasing the pinnacle of POD-like activity at pH 4.5 among the iron-based nanozymes (Fig. S17), its distinguished efficacy in catalyzing •OH generation from H_2O_2 was attributed to its intrinsic catalytic selectivity. This nuanced insight accentuates the pivotal role of catalytic selectivity in augmenting the efficiency of HCFe as a mono-POD nanozyme in tumor catalytic therapy.

Unraveling the selective catalytic mechanism of HCFe nanozyme

Theoretical calculations provide insights into physicochemical properties, chemical reaction thermodynamics, and kinetics. These analyses are pivotal in elucidating the regulation mechanisms of hemin's catalytic activity by various amino acids. Notably, our findings indicate that cysteine coordination significantly reduces the CAT activity of hemin–cysteine, leading to a predominant POD activity, as illustrated in (Fig. 2d).

The core of CAT-like catalytic reaction is the disproportionation of H_2O_2, which is fundamentally a process where electrons are transferred between H_2O_2 molecules. The equations for the overall reaction and its associated two half-reactions are detailed in Fig. 5a. Gao et al. postulated that for a catalyst to participate in the electron transfer of this disproportionation, it must possess an accessible frontier orbital with a reduction potential lying between the potentials of the two half-reactions: specifically, between $\varphi(O_2, H^+/H_2O_2)$ of 0.29 V and $\varphi(H_2O_2, H^+/H_2O)$ of 1.36 V[31,32]. This mediating frontier orbital can either be the highest occupied molecular orbital (HOMO) or the lowest unoccupied

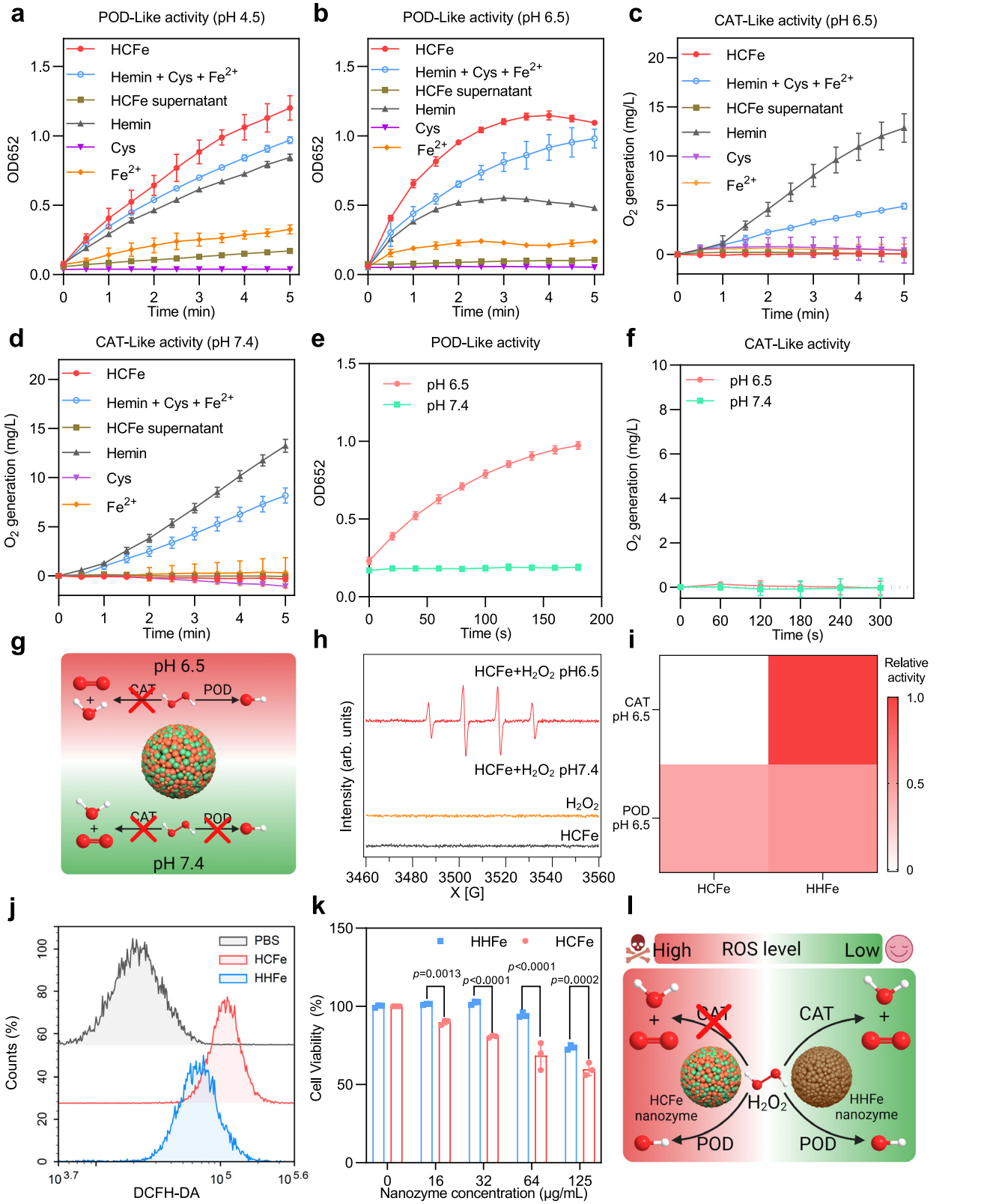

molecular orbital (LUMO). Here, we determined the energy levels of HOMO and LUMO for hemin coordinated with 20 amino acids and converted these levels to potentials relative to a normal hydrogen electrode (E_{NHE}), and the results are presented in Fig. 5a. Our results, presented in Fig. 5a, show that the hemin-based nanozymes in our study utilizes its HOMO to facilitate H_2O_2's disproportionation. This is evident as the reduction potentials of their HOMOs lie between the two aforementioned half-reaction potentials $\varphi(O_2, H^+/H_2O_2)$ and $\varphi(H_2O_2, H^+/H_2O)$. This electron transfer process, as depicted by arrows in Fig. 5a, comprises two steps. The first step is that HOMO donates electrons to H_2O_2, reducing it to water. In the second step, HOMO gains electrons from another H_2O_2 molecule to oxidize it to O_2. An intriguing observation is depicted by the blue dashed line in Fig. 5a, which signifies Hemin's native HOMO. Amino acids influence the

Fig. 4 | Catalytic performance of HCFe mono-POD nanozyme. a, **b** Reaction-time curves of the TMB colorimetric reaction catalyzed by HCFe nanozyme, hemin + cysteine + Fe^{2+} mixture, HCFe supernatant, hemin, Fmoc-L-cysteine or Fe^{2+} at pH 4.5 (**a**) and pH 6.5 (**b**) ($n = 3$ independent experiments). **c**, **d** O_2 produced in H_2O_2 solution containing HCFe nanozyme, hemin + cysteine + Fe^{2+} mixture, HCFe supernatant, hemin, Fmoc-L-cysteine or Fe^{2+} at pH 6.5 (**c**) and pH 7.4 (**d**) ($n = 3$ independent experiments). **e** Reaction-time curves of the TMB colorimetric reaction catalyzed by HCFe nanozyme at pH 6.5 or pH 7.4 ($n = 3$ independent experiments). **f** Dissolved O_2 generated in H_2O_2 solution after being catalyzed by HCFe nanozyme at pH 6.5 or pH 7.4 ($n = 3$ independent experiments). **g** Schematic diagram of the HCFe nanozyme to catalyze the formation of ·OH from H_2O_2 only at pH 6.5, created in BioRender. Jiang (2024) BioRender.com/n42p114. **h** ESR spectra of HCFe nanozyme by using DMPO as spin-trapping agents for detecting ·OH at pH 6.5 and pH 7.4. **i** Comparison of Pod-like activity and CAT-like activity between HCFe and HHFe at pH 6.5. **j** ROS generation in EC109 cells treated with PBS, 200 μg/mL HCFe nanozymes, and 200 μg/mL HHFe nanozymes for 4 h. **k** Cell viability of EC109 cells treated with HCFe and HHFe nanozymes for 48 h ($n = 3$ independent experiments, p values are determined with two-way ANOVA). **l** Schematic diagram of the HCFe nanozyme and HHFe nanozyme to catalyze H_2O_2 in the tumor cell, created in BioRender. Jiang (2024) BioRender.com/v51i451. Data are presented as mean ± SD. Source data are provided as a Source Data file.

hemin's HOMO level through electron-donating or withdrawing effects. Of particular note, cysteine coordination raises the HOMO of hemin–cysteine, decreasing its reduction potential to 0.27 V. This value is slightly below the half-reaction potential $\varphi(O_2, H^+/H_2O_2)$ of 0.29 V. Consequently, this impedes the second electron transfer step, explaining the diminished CAT-like activity of hemin–cysteine. In contrast, the HOMOs of hemins coordinated with amino acids other than cysteine lie between the reductive potentials of the two half-reactions, facilitating the disproportionation of H_2O_2. This observation aligns with our experimental data.

Cysteine may influence the HOMO of hemin by facilitating electron transfer to hemin's Fe atom. To substantiate this proposition, we calculated charges on Fe atoms across 20 distinct nanozymes via natural population analysis (NPA). Figure 5b displays the calculated NPA charges. Notably, the NPA charge of Fe in hemins coordinated by amino acids other than cysteine averages around 1.26. In contrast, cysteine promotes significant electron transfer to the Fe atom, reducing the NPA charge of Fe to 0.63. To elucidate the interaction dynamics between cysteine and hemin, and to discern the directionality of electron transfer, we employed the ETS-NOCV method[33]. As illustrated in Fig. 5b's lower panel, hemin–cysteine can be segregated into two components: Hemin and cysteine. Two primary orbital interactions emerge between these fragments: the interaction between the $3p_z$ orbital of S in cysteine and the $3d_{z2}$ orbital of Fe in hemin, and the interaction between the $3p_x$ orbital of S and the $3d_{xz}$ orbital of Fe. The deformation charge density distribution ($\Delta\rho_{orb}$) corresponding to this orbital interaction denotes the charge flows from cysteine to hemin. Interaction energy contributions from these interaction modalities amount to −126.0 kJ/mol and −125.7 kJ/mol, respectively. Collectively, the data underscores cysteine's pronounced electron-donating propensity to hemin. The Fe K-Edge EXAFS analysis also indicates a decrease in the average oxidation state of Fe in HCFe, consistent with the NPA results (Fig. 3j). These evidence collectively demonstrate electron transfer from Cysteine to hemin, thereby elevating the HOMO of hemin. The elevation of hemin's HOMO hinders its ability to mediate the electron transfer in the H_2O_2 disproportionation reaction, resulting in a loss of its CAT-like activity.

We further delved into the POD- and CAT-like catalytic mechanisms of hemin-amino-acids nanozyme systems through the lens of chemical reaction thermodynamics and kinetics. Figure 5c delineates the HOMO-mediated mechanisms underpinning the POD- and CAT-like activities of nanozymes, extrapolated from our preceding research[34,35]. Intriguingly, the HOMO-mediated mechanisms for both POD and CAT activities share a common initial step: electron transfer from the nanozyme to H_2O_2, generating monatomic oxygen O* (* denotes the adsorbed state). The divergence occurs in the subsequent step, where the substrate dictates the activity—TMB leading to POD-like activity, and H_2O_2 to CAT-like activity. For the POD-like nanozymes, an energy-based descriptor, the adsorption energy of hydroxyl radical $E_{ads,OH}$, was introduced to predict the POD-like activities of nanozymes.[36]. In previous work[35], Gao and collaborators combined the Brønsted–Evans–Polanyi (BEP) relationship with chemical reaction kinetics principles to develop a "volcano model" for nanozymes' POD-like activity. They identified $E_{ads,OH}$, the adsorption energy of hydroxyl radicals on nanomaterials, as a key descriptor. They proposed a universal mechanism that involves H_2O_2 dissociating on the nanomaterial surface to form two adsorbed OH* species (step 1), which then abstracts hydrogen atoms from organic substrates (steps 2 and 3). The rate-determining step varies between steps 1 and 3, with adsorbed OH* as the critical intermediate. This model quantitatively aligns with the Sabatier principle, explaining why highly reactive nanomaterials can become poisoned by strong OH* adsorption, while inert catalysts cannot activate the O–O bond. The highest apparent reaction rates occur with moderate OH* adsorption. By calculating $E_{ads,OH}$, this model can predict H_2O_2 activation activity and rate-determining steps for various materials, providing a simple and universal theoretical basis for nanozyme design and screening. This descriptor subsequently facilitated the strategic design of POD-like nanozymes[37,38]. In our study, we calculated the adsorption-free energies of hydroxyl radical ($G_{ads,OH}$) for the 20 amino acid-coordinated hemin nanozymes, aiming to discern the correlation between $G_{ads,OH}$, and POD-like activities. As depicted in Fig. 5d, there is a conspicuous 'volcano' trend in the nanozyme's POD-like activity, with $G_{ads,OH}$ ranging from −1.38 eV to −0.17 eV. This trend intimates that amino acids have the potential to modulate the $G_{ads,OH}$ of hemin, subsequently influencing its POD activity. This observation underscores the predictive utility of $G_{ads,OH}$: excessively weak adsorption to •OH impedes the O–O bond cleavage in H_2O_2, curtailing POD-like activity, while excessively strong adsorption, although promoting O-O bond breakage in H_2O_2, hinders desorption from the active center, similarly compromising POD-like activity. Optimal POD-like activity is attained when adsorption strength is moderate. Notably, within the scope of our study, hemin–Asn manifested the most pronounced POD-like activity at a pH of 6.5, corresponding to a $G_{ads,OH}$ of −0.58 eV.

To delve deeper into the thermodynamics and kinetics of HOMO-mediated mechanisms underlying the POD- and CAT-like activities of hemin–Cysteine, we calculated the corresponding energy profiles. Figure 5e presents the catalytic cycles alongside the derived energy profiles. Our calculations indicate that electrons transfer from hemin–cysteine to H_2O_2, resulting in the formation of O*, is exothermic, and possesses an activation energy barrier of 0.81 eV. This reaction is feasible at ambient temperature, aligning with the findings in Fig. 5a. However, during the second step in the CAT mechanism, O* faces challenges in capturing a hydrogen atom from the adjacent H_2O_2 due to a substantial energy barrier of 1.57 eV. This phenomenon can be attributed to the HOMO potential being inferior to that of half reaction 1. However, for the second step in the POD mechanism, both O* and OH* exhibit the capability to seize hydrogen atoms from TMB, given their energy barriers of 0.76 eV and 0.89 eV, respectively. The rate-determining step (RDS) in the POD mechanism is the last step, wherein OH* captures hydrogen from TMB. As evidenced in the volcano plot, hemin–cysteine is situated on the left, indicating that its rate-determining step (RDS) involves hydroxyl desorption. Given the energy barrier for this process is a mere 0.89 eV, it underscores hemin–cysteine's prominent POD-like activity.

https://doi.org/10.1038/s41467-024-54868-w

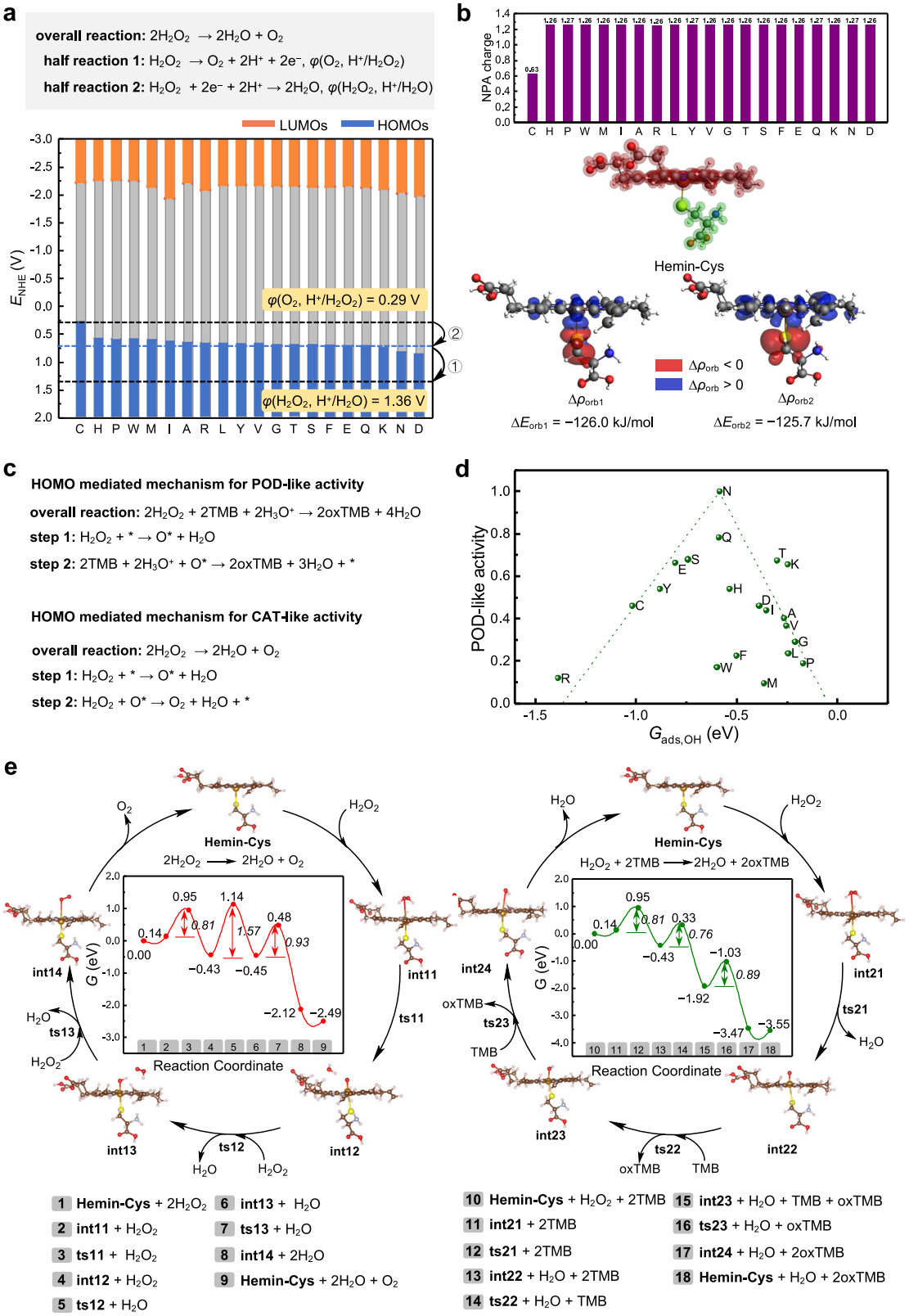

Fig. 5 | The selective catalytic mechanism of HCFe nanozyme. a The equations of the overall reaction and the two half-reactions for H_2O_2 disproportionation reaction and the potentials of HOMO and LUMO energy levels of the 20 amino acid-coordinated hemin relative to a normal hydrogen electrode. **b** The calculated NPA charges on Fe atoms in 20 amino acid-coordinated hHemin based on natural population analysis. **c** The HOMO-mediated mechanisms for POD- and CAT-like activities of nanozymes. **d** The volcano plot of POD-like activities of 20 amino acid-coordinated hemin along with $G_{ads,OH}$ in eV. **e** The catalytic cycles and the corresponding free energy profiles (in eV) for the CAT and POD mechanisms of hemin–cysteine. Amino acids are represented by single-letter abbreviations.

In conclusion, our DFT analyses elucidate why hemin–cysteine predominantly exhibits POD-like activity. The electron transfer from cysteine to hemin elevates its HOMO. This elevation impairs its ability to mediate electron transfer in the H_2O_2 disproportionation reaction, leading to the cessation of its CAT-like activity. The modulation of the hemin's adsorption energy towards the hydroxyl radical by various amino acids further shapes its POD-like catalytic properties.

Combining the results of DFT calculations (Fig. 2b), XPS, and Fe K-Edge EXAFS (Fig. 3), we determined that there are two iron centers in the HCFe nanozyme: Fe–N_4S and Fe–O_4. The sulfur (S) of Fmoc–cysteine bridges with the iron (Fe) in hemin to form Fe–N_4S, while the iron ion coordinates with the carboxyl group to form Fe–O_4. To investigate whether Fe–O_4 is a catalytically active site, we synthesized a control nanozyme, referred to as CFe, assembled using Fmoc-L-cysteine and Fe^{2+}. Unlike HCFe, CFe lacks the hemin component and, therefore, does not contain the Fe–N_4S structure. However, theoretically, CFe should retain the Fe–O_4 structure due to the coordination between Fe^{2+} and carboxyl groups. We evaluated both the POD-like and CAT-like activities of CFe and observed that CFe exhibited neither activity, suggesting that the Fe–O_4 structure does not serve as a catalytic active site (Fig. S18a, b).

DFT calculations were also conducted to investigate the CAT- and POD-like activities of CFe. The CFe model, shown in Fig. S18c, consists of one Fe^{2+} ion coordinated with four cysteine anions. As illustrated in Fig. 5e, the initial steps for both CAT and POD activities involve the adsorption and decomposition of H_2O_2. The energy profiles for these steps at the Fe–O_4 site in the CFe model revealed that the H_2O_2 adsorption energy was 0.23 eV, while the decomposition energy barrier was 2.16 eV (Fig. S18d), significantly higher than that at Fe–N_4 sites. This indicates the poor ability of Fe–O_4 sites to activate H_2O_2, leading to the low CAT- and POD-like activities of CFe. These results support experimental observations and provide detailed insights at the atomic level to suggest that the Fe–O_4 structure does not serve as a catalytic active site.

Furthermore, we employed ICP-MS to analyze the Fe content in 20 biomimetic iron-based nanozymes, including HCFe. The results indicate that the Fe content across these nanozymes is relatively consistent, with the HCFe nanozyme displaying a Fe content of approximately 10.5026%, placing it in the median range among the tested nanozymes (Table S7). This consistency suggests that the Fe content does not influence the catalytic selectivity of these biomimetic iron-based nanozymes. These findings suggest that the unique catalytic properties of the HCFe nanozyme are related to the Fe–N_4S structure formed by the interaction of Fmoc-L-cysteine with hemin.

HCFe nanozyme combined with CDDP overcame the CDDP-resistance in esophageal squamous cell carcinoma cells

After deciphering the mechanism by which the nanozyme exhibits POD-like catalytic specificity, we proceeded to evaluate its application in tumor catalytic therapy. The inherent heterogeneity and multifaceted nature of tumors have rendered single-treatment strategies ineffectual, necessitating a paradigm shift towards multimodal therapeutic regimens in oncological management[39]. Chemotherapy is a pivotal modality in cancer treatment, yet its efficacy is severely hindered by the pervasive challenge of resistance[40,41]. This resistance is intricately linked with the modulation of reactive oxygen species (ROS) in tumor cells, augmentation of ROS levels within tumor cells emerges as a strategy to amplify chemotherapeutic responsiveness[42–44]. Remarkably, the nanozyme remains inert in a neutral pH physiological environment and exhibits specific POD-like activity in the mildly acidic tumor microenvironment, catalyzing the generation of ROS to destroy tumor cells. This distinct operational modality not only underscores its biosafety but also accentuates its therapeutic potency. Against this backdrop, integrating nanozymes with chemotherapy is proposed as a viable strategy, promising enhanced efficacy. To substantiate this proposition, our investigation employed a model comprising cisplatin-resistant esophageal squamous cell carcinoma (ESCC), utilizing cisplatin (CDDP) as a representative chemotherapeutic agent. This approach facilitated an in-depth exploration of the synergistic effects elicited by the concomitant application of nanozymes in a chemotherapeutic context, potentially offering a nuanced understanding and avenues to surmount chemotherapy resistance.

Firstly, we established three CDDP-resistant ESCC cell lines from parent ESCC cell lines EC109, EC9706, and TE1 (Fig. 6a). Cell viability assays revealed a marked increase in drug tolerance in the resistant lines compared to their parent counterparts (Fig. 6b–d), with IC50 values indicating enhanced cisplatin resistance (Table S8). RNA sequencing of EC109 and EC109DDP cells identified 852 upregulated and 854 downregulated genes in the resistant strain (Fig. 6e). Notably, the overexpression of genes associated with platinum efflux (ABCC2 and ABCC3) and glutathione-mediated detoxification (Nrf2, GPX4, and GST) was observed (Fig. 6f), hinting at a multifaceted resistance mechanism. Analyses of intracellular platinum concentrations showcased significant reductions in EC109DDP, EC9706DDP, and TE1DDP cells post-cisplatin exposure (Fig. 6g), aligning with an augmented glutathione content (Fig. 6h). Western blot analyses corroborated the RNA sequencing data, showing elevated levels of MRP2, Nrf2, and GPX4 proteins in resistant cell lines (Fig. 6i). Enhanced DNA repair and reduced apoptosis in the resistant cells were further demonstrated by the subdued expression of γ-H2AX and Cleaved-caspase 3, following cisplatin treatment, compared to the pronounced responses in the parent cells (Fig. S19). The concomitant reduction in apoptotic rates in resistant cells underpins the enhanced tolerance to cisplatin-induced oxidative stress and cell injury (Fig. S20). In essence, the augmented cisplatin tolerance in ESCC is potentially orchestrated by enhanced platinum efflux, increased glutathione-mediated detoxification, and bolstered antioxidant defenses, collectively mitigating oxidative stress-induced cellular damage and apoptosis.

We subsequently investigated the cytotoxic effects of HCFe nanozyme in combination with CDDP on CDDP-resistant ESCC cells. Quantitative analysis revealed that this combination elicited a markedly higher cytotoxic response compared to either HCFe nanozyme or CDDP alone across all three ESCC cisplatin-resistant cell lines (Fig. 7a–c). The combination indexes (CI) underscored a synergistic effect between HCFe nanozyme and CDDP (Fig. 7d). Furthermore, cell apoptosis analyses corroborated the synergistic impact of this combination, showing enhanced apoptosis in both the cisplatin-resistant ESCC cells and their corresponding parental cells (Figs. S21 and S22). Additionally, the ROS scavenger NAC was able to counteract the enhanced cytotoxic response and increased cell apoptosis of the CDDP + HCFe treatment. This further substantiates that the synergistic effect between HCFe nanozyme and CDDP relies on ROS generation by HCFe nanozymes.

RNA sequencing data elucidated minimal changes in gene expression in EC109DDP cells post-5μM CDDP treatment for 48 h, highlighting the cells' resilience against CDDP (Fig. 7e). In stark contrast, combined HCFe and CDDP treatment instigated significant modulations in gene expressions, marking a potential mechanistic shift imparted by HCFe (Fig. 7e). Notably, downregulation of chemotherapy-resistant genes in the ABC family hinted at HCFe's inhibitory action on CDDP efflux (Fig. 7f).

An upsurge in ROS levels was observed in EC109DDP cells treated with HCFe, both as a standalone treatment and in combination with CDDP, as indicated in Figs. 7g and S11. NAC, employed as a free radical scavenger, effectively nullified ROS augmentation induced by HCFe, corroborating the ROS-centric action of HCFe (Figs. 7g and S23).

In parallel, HCFe instigated a discernible decline in mitochondrial membrane potential, as evidenced by JC-1 fluorescence imaging (Figs. 7h and S24), implicating mitochondrial damage as a consequence of elevated ROS. The combined HCFe and CDDP treatment

https://doi.org/10.1038/s41467-024-54868-w

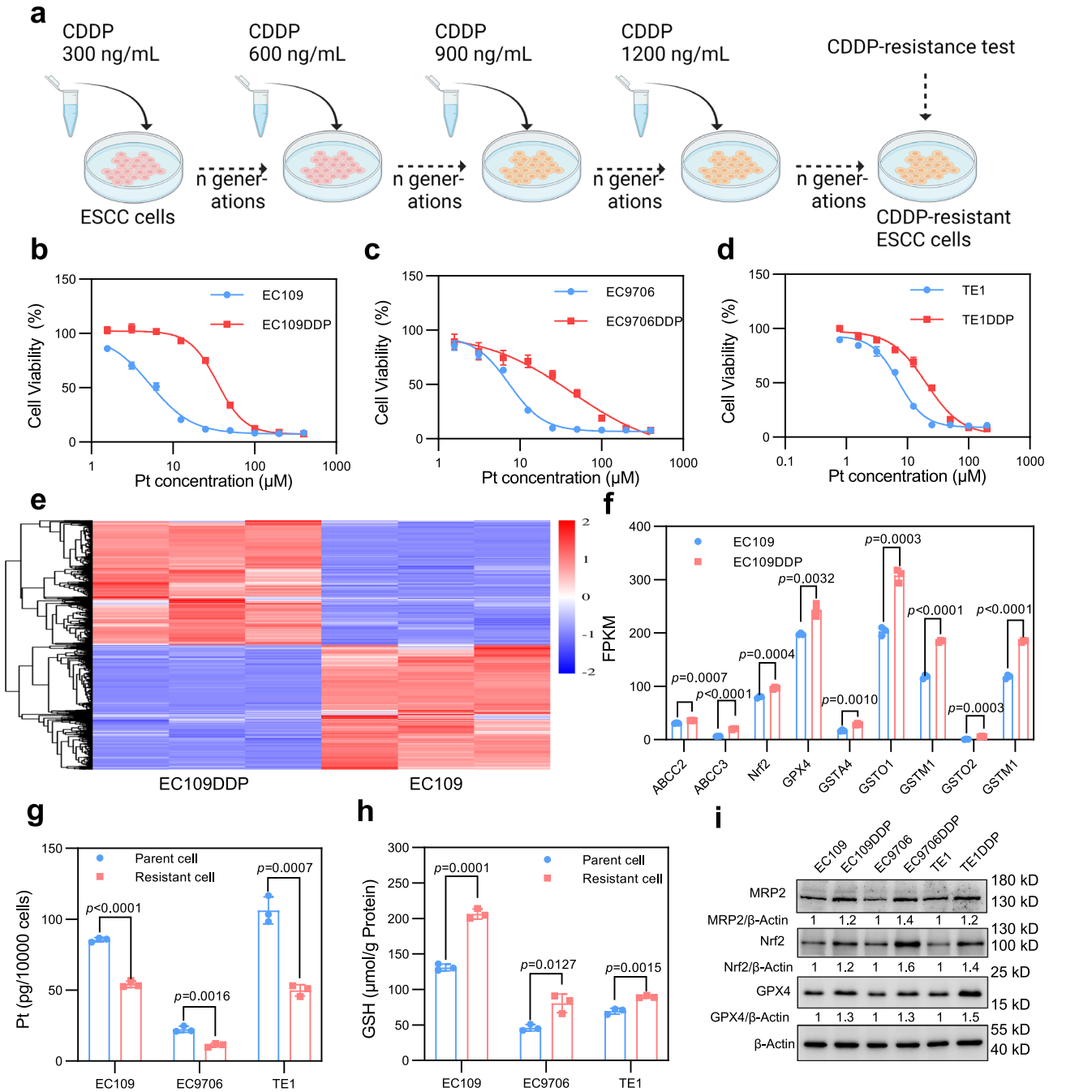

Fig. 6 | Characteristics of esophageal squamous cell carcinoma CDDP resistant cells. a The schematic illustration of establishments of CDDP-resistant ESCC cell lines, created in BioRender. Jiang (2024) BioRender.com/q47h357. Cell viability of **b** EC109 and EC109DDP, **c** EC9706 and EC9706DDP, and **d** TE1 and TE1DDP cells treated with CDDP for 48 h ($n = 3$ independent experiments). **e** The differentially expressed genes (DEGs) of EC109DDP and EC109 cells were measured by RNA-seq ($n = 3$ independent experiments). **f** The DEGs of interest between EC109DDP and EC109 cells ($n = 3$ independent experiments, p values are determined with two-tailed unpaired student's t-test. FPKM fragments per kilobase of exon model per million mapped fragments). **g** The intracellular Pt concentrations of CDDP-resistant cells (EC109DDP, EC9706DDP, and TE1DDP) and parent cells (EC109, EC9706, and TE1) incubated with CDDP (10 μM) for 5 h were determined by ICP MS ($n = 3$ independent experiments, p values are determined with two-tailed unpaired student's t-test). **h** Cellular GSH levels in CDDP-resistant cells and parent cells ($n = 3$ independent experiments, p values are determined with two-tailed unpaired student's t-test). **i** Western blot analysis of MRP2, Nrf2, and GPX4 expressions in CDDP-resistant cells and parent cells. Data are presented as mean ± SD. Source data are provided as a Source Data file.

precipitated increased cytoplasmic cytochrome C levels, an upsurge nullified by NAC, while concomitantly depleting ATP content, a decrease also counteracted by NAC (Figs. 7i and S25). This outcome underscores the capability of HCFe nanozyme to inflict mitochondrial damage and reduce ATP content via the amplification of cellular ROS.

It is well documented that an increase in ROS can suppress the expression of multidrug resistance protein (MRP), thereby enhancing cellular responsiveness to chemotherapy drugs[45,46]. Given the association between multidrug resistance protein 2 (MRP2) and ESCC cisplatin resistance[41,47], we observed a significant reduction in MRP2 expression following HCFe treatment (Figs. 7j and 6k), suggesting a

https://doi.org/10.1038/s41467-024-54868-w

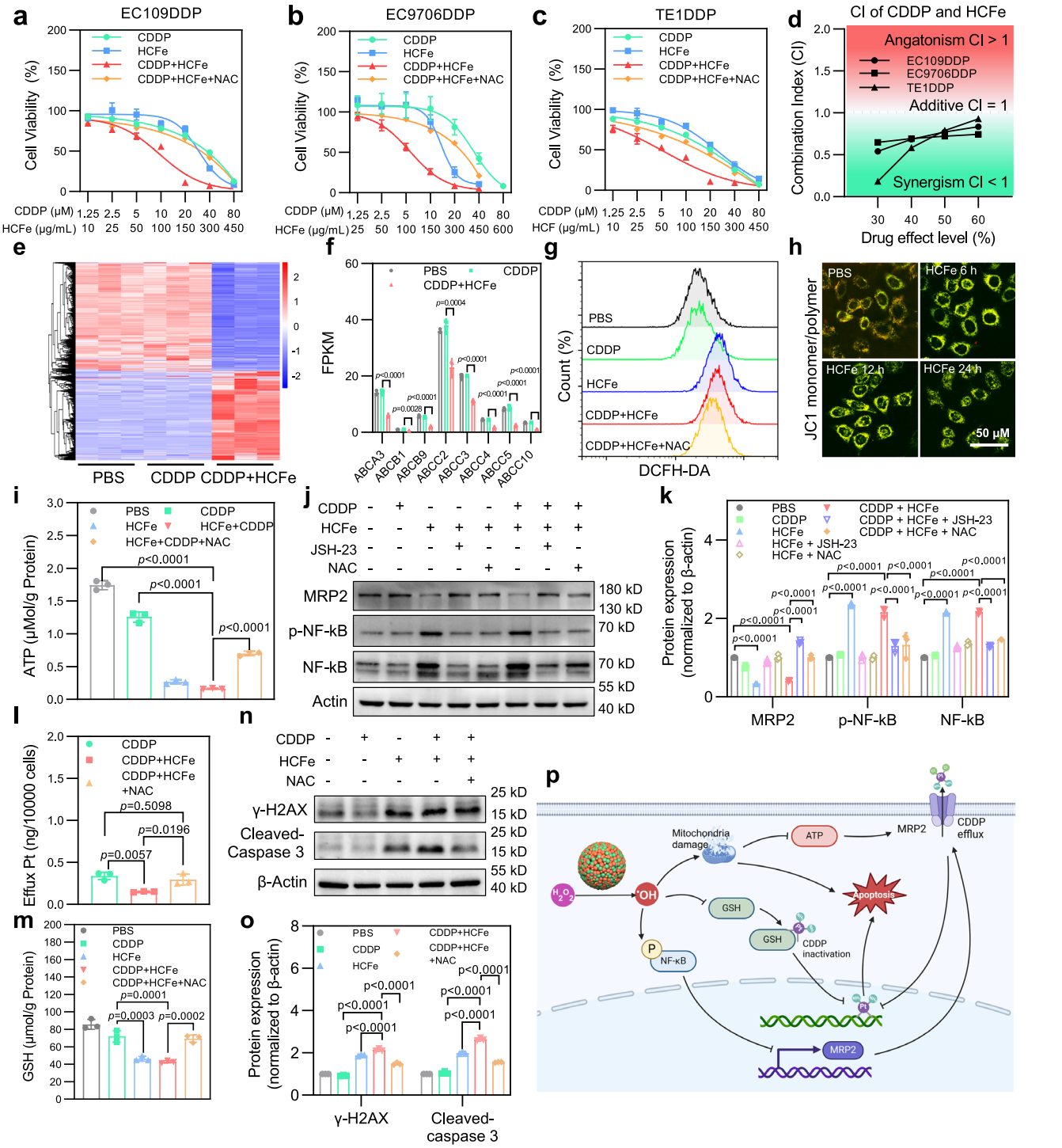

Fig. 7 | HCFe nanozyme combined with CDDP overcame the CDDP resistance in esophageal squamous cell carcinoma cells. a–**c** Cell viability of EC109DDP, EC9706DDP, and TE1DDP cells with different treatments for 48 h. **d** Combination index (CI) of CDDP and HCFe nanozyme against EC109DDP, EC9706DDP, and TE1DDP cells (CI < 1: synergism; CI = 1: additive effect; CI > 1: antagonism). **e** Differentially expressed genes (DEGs) of EC109DDP cells treated with PBS, 5 μM CDDP, 75 μg/mL HCFe, and 5 μM CDDP + 75 μg/mL HCFe for 48 h, measured by RNA-seq. **f** Expression levels of ABC transporter family genes in EC109DDP cells after different treatments (*p* values are determined by one-way ANOVA. FPKM fragments per kilobase of exon model per Million mapped fragments). **g** ROS generation in EC109DDP cells with different treatments for 6 h. **h** Mitochondrial membrane potential (MMP) changes in EC109DDP cells treated with 150 μg/mL HCFe for 6 h, 12 h, and 24 h, assessed by JC-1 staining (red: JC-1 polymer; green: JC-1 monomer). Scale bar = 50 μm. **i** ATP content analysis in EC109DDP cells after 24 h of treatment. (*p* values are determined by two-way ANOVA). **j**, **k** Western blot analysis (**j**) and quantitative assessment (**k**) of phosphorylated NF-κB, NF-κB, and MRP2 in EC109DDP cells (*p* values are determined by two-way ANOVA). **l** Platinum efflux and **m** intracellular GSH levels in EC109DDP cells (*p* values are determined by one-way ANOVA). **n**, **o** Western blot and quantitative analysis of γ-H2AX and Cleaved-caspase 3 expressions in EC109DDP cells after 24 h of treatment (*p* values are determined by two-way ANOVA). **p** Schematic illustration of the mechanism by which excessive ROS overcomes cisplatin resistance, created in BioRender. Jiang (2024) BioRender.com/p01k654. Cells were treated with PBS, 10 μM CDDP, 150 μg/mL HCFe, 10 μM CDDP + 150 μg/mL HCFe, or 10 μM CDDP + 150 μg/mL HCFe + 5 mM NAC in panels (**g**, **i**, **l**, **m**, and **n**). *n* = 3 independent experiments in panels (**a**–**c**), (**f**), (**i**–**o**). Data are presented as mean ± SD. Source data are provided as a Source Data file.

potential inhibition of cisplatin efflux. This assertion is substantiated by the data demonstrating a marked reduction in CDDP efflux in EC109DDP cells subjected to combined HCFe and CDDP treatment (Fig. 7l). Furthermore, this reduction in CDDP efflux in EC109DDP cells could be counteracted by NAC treatment.

NF-κB, which is influenced by ROS, may drive MRP2 downregulation[48]. High ROS levels are known to activate NF-κB[49]. Based on these insights, we propose that treatment with CDDP + HCFe could generate excessive ROS, thereby enhancing NF-κB expression and contributing to MRP2 downregulation. This theory is corroborated by transcriptomic sequencing results showing an increase in NF-κB mRNA and a decrease in MRP2 mRNA levels following treatment (Fig. S26). Protein expression analyses revealed that both HCFe and CDDP + HCFe treatments increased NF-κB activation and reduced MRP2 protein levels (Fig. 6j, k). Using the NF-κB inhibitor JSH-23 and the ROS scavenger NAC, we confirmed that these changes were due to ROS influencing the NF-κB/MRP2 pathway. These interventions reversed the changes in protein expression, reducing elevated phosphorylated NF-κB levels and MRP2 depletion. Thus, HCFe nanozyme likely enhances NF-κB activation by inducing excessive ROS, which suppresses MRP2 expression.

Acknowledging the elevated GSH levels characteristic of cisplatin-resistant ESCC cells and the ROS-reducing capacity of GSH, we evaluated cellular GSH levels in EC109DDP cells administered with CDDP alone or in combination with HCFe nanozyme. A marked depletion in GSH levels was noted in the combination treatment group, an effect reversible by NAC (Fig. 7m), underscoring the ROS-inducing and GSH-scavenging properties of HCFe nanozyme. Furthermore, this combined treatment strategy augmented the expression of γ-H2AX and cleaved-caspase 3, indicative of enhanced DNA damage and apoptosis, effects partially reversible by NAC (Figs. 7n and 6o), as confirmed by apoptosis assays (Figs. S21 and S22).

Consequently, we deduced that HCFe nanozyme primarily ameliorates ESCC cisplatin resistance by instigating excessive ROS, which in turn curtails CDDP efflux, depletes cellular GSH, and augments DNA damage and cell apoptosis (Fig. 7p).

HCFe nanozyme combined with CDDP for CDDP-resistant ESCC tumor therapy in vivo

To evaluate the biodistribution of HCFe nanozyme, EC109DDP tumor-bearing female BALB/c nude mice were administered HCFe–Cy5.5 via tail vein injection. The in vivo imaging system showcased the nanozyme's pronounced tumor enrichment, revealing an extended retention compared to free Cy5.5 (Fig. S27a). Quantitative fluorescence data confirmed elevated signals in the tumor area for the HCFe–Cy5.5 group, persisting for 96 h post-injection (Fig. S27b). Ex vivo imaging further supported the nanozyme's effective tumor targeting and retention capabilities (Fig. S27c, d).

Safety assessments were performed to explore the biosafety profile of HCFe nanozyme and CDDP. Female BALB/c mice treated with various doses of HCFe nanozyme (20 mg/Kg, 50 mg/Kg, and 100 mg/Kg) exhibited stable body weight, confirming its safety (Fig. 8a). In contrast, higher CDDP doses resulted in significant weight loss, indicating toxicity, while a dose of 2.5 mg/Kg CDDP was deemed safe. Combining 2.5 mg/Kg CDDP with different concentrations of HCFe nanozyme, administered via tail vein, presented no significant change in body weight, further attesting to the combined treatment's biosafety (Fig. 8a).

The comprehensive safety profile was supplemented with blood biochemistry and routine blood analyses, wherein all indices from various treatment groups remained within normal parameters (Fig. 8b–e and Table S9). Histological examinations, employing H&E staining of principal organs (heart, liver, spleen, lung, and kidney), revealed no discernible tissue damage, substantiating the combined treatment's biological safety (Fig. S28).

The in vivo antitumoral efficacy was explored by treating cisplatin-resistant ESCC xenografts with saline, 2.5 mg/Kg CDDP, 50 mg/Kg HCFe nanozyme, or a combination of 2.5 mg/Kg CDDP and 50 mg/Kg HCFe nanozyme every three days, thrice (Fig. 8f). The cisplatin treatment group did not exhibit a significant reduction in tumor growth compared to the saline group, confirming the cisplatin resistance of EC109DDP cell-derived xenografts (Fig. 8g, h, and i). In contrast, the co-administration of HCFe nanozyme and CDDP markedly suppressed the proliferation of cisplatin-resistant ESCC xenografts, suggesting the potential of this combined approach to counteract cisplatin resistance (Fig. 8g–k). At the end of the experiment, on the 21st day after the initial treatment, tumor tissues were collected, photographed, and weighed. The tumor volume and weight in the combined treatment group were significantly lower compared to the control group and the groups treated with a single drug, as shown in Fig. 7l, m.

Moreover, akin to the safety profile observed in prior experiments, no substantial weight loss was recorded across the treatment groups, underscoring the biosafety of the HCFe and CDDP combination (Fig. 8n). Notably, female tumor-bearing mice receiving the combined therapy exhibited a significant extended survival duration. By the 28th day, while all female tumor-bearing mice in the other treatment cohorts succumbed, an 80% survival rate was observed in the combined treatment group (Fig. 8o), highlighting the treatment's biosafety and effectiveness. Histological analyses via H&E staining and TUNEL assays revealed pronounced tissue necrosis and apoptosis in tumors from female tumor-bearing mice subjected to the combined HCFe nanozyme and CDDP regimen (Fig. 8p).

Collectively, these findings affirm that the integration of HCFe nanozyme with CDDP not only effectively impedes the growth of cisplatin-resistant ESCC xenografts but also enhances survival rates and biosafety, laying a promising foundation for future therapeutic applications.

In this study, employing a supramolecular assembly approach involving Fmoc-L-cysteine, heme, and Fe^{2+} coordination, we introduced sulfur coordination to the iron atom in hemin, leading to the synthesis of the HCFe nanozyme. This nanozyme uniquely combines heme and Fe–S structures within its catalytic active center. Utilizing a set of 19 Fmoc-modified amino acids as comparative controls, we constructed a comprehensive library of iron-based nanozymes. Subsequent enzymatic activity analysis confirmed HCFe's unique mono-POD activity, distinguishing it from the other 19 variants and hemin with both POD and catalase activities. This analysis further demonstrated that HCFe exceeds the catalytic selectivity of the natural HRP enzyme, which exhibits a slight CAT-like activity. These findings categorize HCFe as a specialized iron-based mono-POD nanozyme.

The HCFe nanozyme was closely examined to understand its structural and functional attributes. HCFe's distinct mono-POD activity and enhanced proficiency in facilitating H_2O_2 catalysis were established against other iron-based nanozymes under an acidic tumor environment, underscoring its unique role and efficiency in tumor catalytic therapy attributed to its intrinsic catalytic selectivity. Using X-ray photoelectron spectroscopy (XPS) and X-ray absorption fine structure spectroscopy (XAFS), we delved deeper into HCFe's structural composition. The results uncovered a complex interplay between iron and sulfur within the nanozyme's structure. The analyses enhanced our grasp of its unique catalytic specificity. Theoretical computations shed light on the role of sulfur coordination in skewing hemin's catalytic inclination towards predominant POD activity.

In the scenario of CDDP-resistant ESCC, HCFe proved its mettle, enhancing chemotherapeutic responsiveness, validated through comprehensive in vitro and in vivo experiments. The synergy of HCFe and CDDP not only proved efficacious but also showcased a

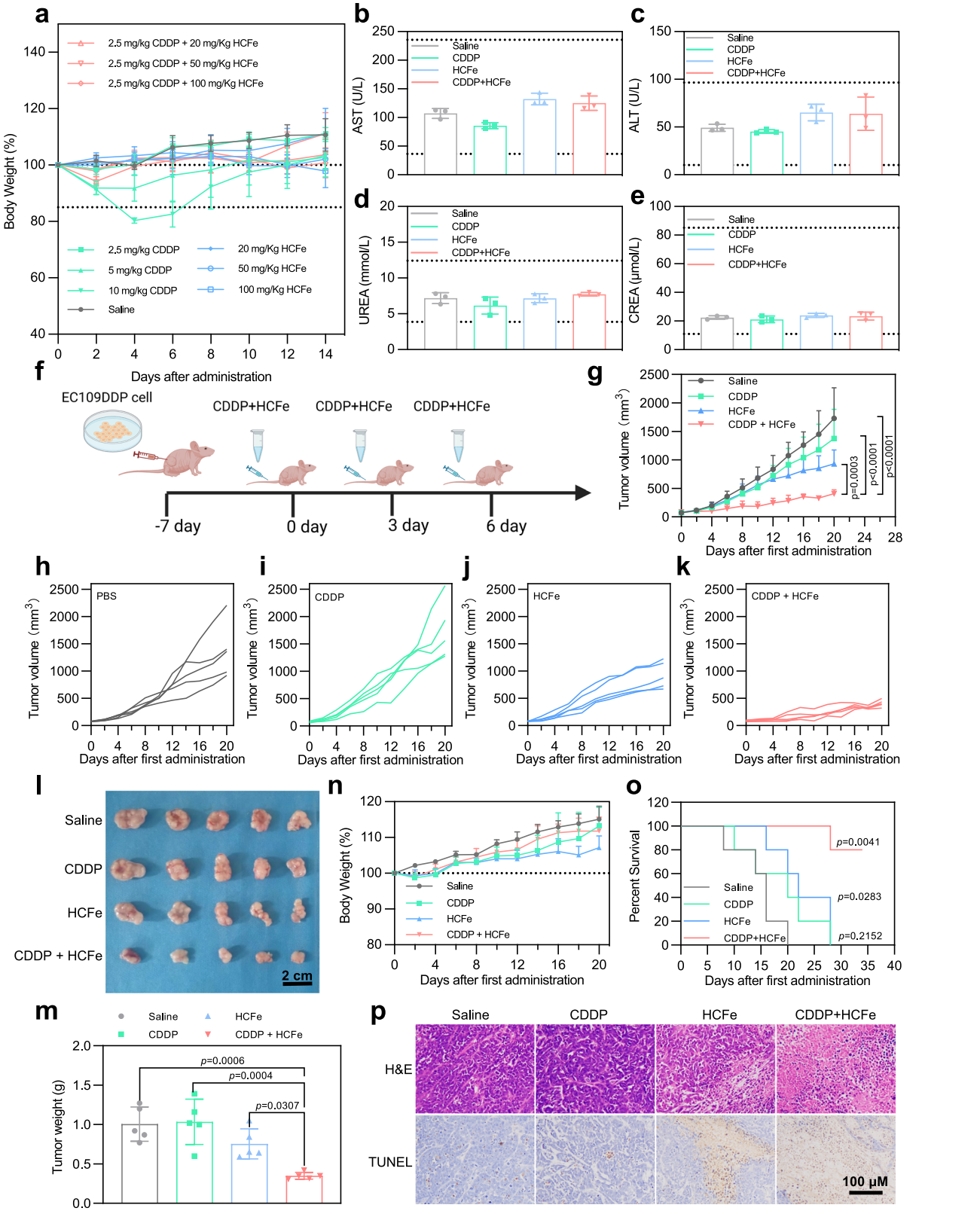

commendable safety profile, as evidenced in studies involving cisplatin-resistant ESCC xenografts.

HCFe nanozyme, characterized by its unique mono-POD activity and the integration of heme and Fe–S structures within its catalytic active center, emerges as a cornerstone for devising innovative therapeutic strategies in cancer therapy. As a type of single-atom nanozyme, HCFe nanozymes also inherit the efficient catalytic capabilities characteristic of previously reported single-atom nanozymes[50–53], which are utilized in catalytic medicine applications. Our study is comprehensive, offering a deep dive into the enzymatic activity of HCFe and exploring its potential to boost the effectiveness of chemotherapy. We delve into avenues for enhancing the catalytic selectivity and specificity of nanozymes. These advancements highlight HCFe's pivotal role in the evolving field of oncology.

Fig. 8 | HCFe nanozyme combined with CDDP for CDDP-resistant ESCC tumor therapy in vivo. a Body weight changes of healthy female BALB/c mice after intravenously administered with CDDP, HCFe nanozyme, and CDDP + HCFe nanozyme at 2.5 mg/kg, 5 mg/kg, 10 mg/kg CDDP equivalent or 20 mg/kg, 50 mg/kg, 100 mg/kg HCFe nanozyme equivalent ($n = 3$ mice per group). **b**–**e** Serum biochemistry data of healthy female BALB/c mice after injected with Saline, 2.5 mg/kg CDDP, 50 mg/kg HCFe nanozyme, or 2.5 mg/kg CDDP + 50 mg/kg HCFe nanozyme for 14 d. AST and ALT represent liver function, and UREA and CREA represent kidney function ($n = 3$ mice per group). **f** Schematic illustration of the establishment of CDDP-resistant ESCC tumor models and the corresponding therapeutic regimens, created in BioRender. Jiang (2024) BioRender.com/p01k654. **g**–**k** Tumor growth curves after first administration ($n = 5$ mice per group, p values are determined with two-way ANOVA). **l** Tumor photographs and **m** weights of different treatment group ($n = 5$ mice per group, p values are determined with one-way ANOVA). **n** Body weight changes after the first administration of saline, 2.5 mg/kg CDDP, 50 mg/kg HCFe nanozyme, or 2.5 mg/kg CDDP + 50 mg/kg HCFe nanozyme ($n = 5$ mice per group). **o** Survival curves of female tumor-bearing mice from different treatment groups ($n = 5$ mice per group, p values are determined with log-rank Mantel-Cox test compared with Saline group). **p** TUNEL and H&E staining images of tumor tissue slices collected from female tumor-bearing mice with different treatments after execution. Scale bar = 100 μm. Data are presented as mean ± SD. Source data are provided as a Source Data file.

Methods

Ethical regulations

All research complied with the relevant ethical regulations. The animal studies were conducted in accordance with the ethical standards set by the Animal Ethics Committee of Zhengzhou University (approval number: ZZUIRB2022-144). Female BALB/c nude and healthy mice, aged 6–8 weeks, were sourced from SPF (Beijing) Biotechnology Co., Ltd. All mice were group housed 5 mice per cage in a specific pathogen-free environment temperature (22–26 °C) and humidity (40–70%) house rooms on a 12 h light, 12 h dark cycle. The Animal Ethics Committee permits a maximum tumor size of 2000 mm^3, we terminated the in vivo therapy assay when the tumor arrived at this size in this work. According to the Animal Ethics Committee guidelines, mice that experience weight loss exceeding 20% or display symptoms such as hunched posture, impaired locomotion, or respiratory distress should be promptly euthanized using CO_2 gas. Otherwise, the mice were euthanized at the conclusion of the experiment. In the 10 mg/kg CDDP group, one mouse exceeded the permitted weight loss limit of 20% on Day 4, with a recorded body weight of 79.81% of its initial weight. The mouse was observed to be in good health with normal behavior, so euthanasia was not performed, and observation continued under the guidance and approval of the veterinarian. In the Saline group, one mouse exceeded the permitted tumor burden limit of 2000 mm^3 on Day 18, with a tumor volume of 2139.29 mm^3. However, the mouse was in good health, without signs of distress, and all other mice in the same group had tumor volumes below 1500 mm^3. Based on these observations, and under the veterinarian's approval, we continued monitoring these mice to maintain data integrity, as this decision was necessary to capture comprehensive data on the effects of treatments under investigation. Monitoring included daily health checks, weight measurements, and behavioral assessments to ensure animal welfare.

Cell lines

EC109 cell line and TE1 cell line were purchased from BeNa (Henan, China) Culture Collection Co., Ltd. EC9706 cell line was donated by the Laboratory of Cell Engineering Transformation, College of Life Science, Zhengzhou University. Resistant derivatives, EC109DDP, EC9706DDP, and TE1DDP, were developed from their respective parent cells through a 10-month exposure to incrementally increased concentrations of CDDP. Cells were maintained in RPMI-1640 medium, supplemented with 10% FBS and 1% penicillin/streptomycin, and incubated at 37 °C in a 5% CO_2 humidified atmosphere. The resistant cell lines were sustained in 1.2 μg/mL CDDP to preserve their resistant characteristics.

Preparation of biomimetic self-assembled iron-based nanozymes

The 0.05 mmol hemin and 0.1 mmol Fmoc-L-AA were dissolved in 1 mL DMSO, and 0.1 mmol $FeCl_2{\cdot}4H_2O$ was dissolved in 20 mL ultrapure water. The pre-mixed DMSO solution containing hemin and Fmoc-L-AA was added to the aqueous solution containing $FeCl_2{\cdot}4H_2O$ under slow stirring. After adjusting the pH to about 7.0 with 0.1 M NaOH, the resulting suspension was dialyzed overnight in ultrapure water using a dialysis bag with a molecular weight cut-off of 8k–14k to remove unassembled molecules and ions. Then, the suspension was centrifuged at 15,777×g for 10 min and the precipitate was resuspended with 5 mL ultrapure water. After precooling at −80 °C for 30 min, the suspension was lyophilized in a vacuum freeze dryer. Hemin–Fmoc–AA–Fe self-assembled nanozymes were obtained as powder solids after freeze-drying, and their particle sizes and zeta potential were measured via dynamic light scattering (DLS, Zetasizer pro, Malvern, United Kingdom).

Determination of POD-like activity

The POD-like activity of hemin–Fmoc–AA–Fe nanozymes was assessed using TMB as the substrate in the presence of H_2O_2. Briefly, 10 μL of hemin–Fmoc–AA–Fe nanozymes was added into 90 μL of acetate buffer solution (0.2 M, pH4.5) or phosphate buffer solution (50 mM, pH 6.5 or 7.4) containing 1 μL TMB (20 mg/mL in DMSO) and 5 μL H_2O_2 (10 M). The absorption value at 652 nm of oxidized TMB was continuously recorded via a Tecan Spark multimode reader.

To characterize the kinetic of HCFe nanozyme with H_2O_2 as substrate, the H_2O_2 was added into the reaction at the final concentrations of 0 mM, 7.8125 mM, 15.625 mM, 31.25 mM, 62.5 mM, 125 mM, 250 mM, and 500 mM. The absorbance values at 652 nm were continuously detected by a microplate reader to calculate the initial reaction speed at different H_2O_2 concentrations.

To characterize the kinetic of HCFe nanozyme with TMB as substrate, the TMB was added into the reaction at the final concentrations of 0 mM, 0.05 mM, 0.1 mM, 0.2 mM, 0.4 mM, 0.8 mM, and 1.6 mM TMB. The absorbance values at 652 nm were continuously detected by a microplate reader to calculate the initial reaction speed at different TMB concentrations.

Kinetic constant K_M and V_{max} were determined using GraphPad Prism 7.0 software. The initial reaction rate (v) and substrate concentration [S] were fitted to the Michaelis–Menten equation, expressed as: $v = (V_{max} \times [S])/(K_M + [S])$.

Determination of CAT-like activity

The catalase-like activity was characterized by measuring the rate of dissolved oxygen production in the reaction system using a dissolved oxygen meter. Briefly, Nanozymes and H_2O_2 were mixed in 2 mL of phosphate buffer solution (pH 6.5 or 7.4), and the dissolved oxygen concentrations were detected continuously by a dissolved oxygen meter.

Nanozymes-induced •OH generation measured by ESR

The generation of •OH was quantified using electron spin resonance (ESR) spectroscopy with DMPO as the spin-trapping probe. Briefly, 10 μL of nanozyme solution (0.5 mg/mL) was mixed with 85 μL of phosphate buffer (50 mM, pH 6.5 or 7.4) containing DMPO (5 μL, 1 M), then 5 μL of H_2O_2 (400 mM) were added to start the reaction. The formation of spin-trapped DMPO-•OH adducts was subsequently recorded to confirm the generation of •OH.

Characterization of HCFe nanozyme

The morphology of the HCFe nanozyme was analyzed using TEM (Thermoscientific/Talos L120CG2). The surface elemental distribution

was evaluated via X-ray energy disperse spectroscopy (EDS). High-resolution atomic structure visualization was achieved through aberration-corrected high-angle annular dark-field scanning TEM (AC HAADF-STEM, Titan Cubed Themis G2 300). Hydrodynamic size and zeta potential measurements were performed using dynamic light scattering (DLS, Zetasizer Pro, Malvern, United Kingdom). The iron content was quantified using inductively coupled plasma mass spectrometry (Agilent ICP-MS 7850 instrument), chlorine content was measured through oxygen bomb combustion ion chromatography, and the contents of carbon, nitrogen, hydrogen, and sulfur were determined using organic elemental analysis.

Elemental and chemical bonding information was obtained via X-ray photoelectron spectroscopy (XPS, Thermo EscaLab 250Xi). The coordination environment of the iron center was studied using X-ray absorption near-edge structure (XANES) and extended X-ray absorption fine structure (EXAFS) spectroscopy, performed at the BL16U1 beamline at the Shanghai Synchrotron Radiation Facility (SSFR, 3.5 GeV, 250 mA). Data processing, including reduction, analysis, and EXAFS fitting, was carried out using the Athena and Artemis programs from the Demeter data analysis suite[54], utilizing the FEFF6 program for EXAFS fitting[55]. Energy calibration was performed using standard Fe foil measured simultaneously as a reference. The pre-edge background was subtracted with a linear function, and the edge jump was normalized with Athena software. The χ(k) data were extracted by subtracting a smooth third-order polynomial simulating the atomic absorption background. The k^3-weighted $\chi(k)$ data were Fourier transformed using a HanFeng window function ($\Delta k = 1.0$). For EXAFS modeling, global amplitude parameters (CN, R, σ^2, and ΔE_0) were obtained via nonlinear least-squares fitting of the EXAFS equation in R-space using Artemis. The amplitude reduction factor S_O^2 derived from Fe foil fitting (0.703) was applied to estimate coordination numbers for Fe–N, Fe–S, and Fe–Fe paths in the sample.

Mössbauer spectroscopy was conducted in transmission mode at room temperature using a ^{57}Co (Rh) radioactive γ-ray source. The isomer shifts were calibrated with α-Fe foil. Powdered samples were pressed into a pancake-like shape within a plastic mold and analyzed in the Mössbauer instrument. The spectra were fitted using the least-squares method with a Lorentzian function.

Theoretical calculation characterization of HCFe nanozyme

All the geometric optimizations and free energy calculations were conducted using the Gaussian 09 D.01 package[56]. The B3LYP hybrid functional[57] in conjunction with 6–31 G(d,p) basis sets[58] for non-metal elements and SDD pseudopotential and basis sets[59] for Fe element was applied. The charges were obtained using the natural population analysis method[60]. The orbital interaction between cysteine and hemin moieties was analyzed using the extended transition state–natural orbitals for chemical valence (ETS-NOCV) theory[33]. The Becke–Perdew exchange-correlation functional BP86[61–63] with the TZ2P basis sets as implemented in the ADF2014.10. package[64] was used.

Cytotoxicity assay

To evaluate the resistance of EC109DDP, EC9706DDP, and TE1DDP cells to CDDP, the CDDP-resistant cells (EC109DDP, EC9706DDP, and TE1DDP) and parent cells (EC109, EC9706, and TE1) were respectively seeded in 96-well plates at a density of 6000 cells per well and cultured overnight for adherence. Then, the cells were treated with CDDP at 400 μM, 200 μM, 100 μM, 50 μM, 25 μM, 12.5 μM, 6.25 μM, 3.125 μM, 1.5625 μM, and 0 μM for 48 h. The viability of cells was determined using a CCK-8 assay. The cisplatin resistance index was calculated to determine the degree of tolerance of the resistant cell lines to cisplatin. Cisplatin resistance index (RI) = $IC_{50,\text{resistant cells}}/IC_{50,\text{parent cells}}$, RI values higher than 1 indicate that the cell has become resistant to cisplatin.

To determine the cytotoxicity of CDDP combined HCFe nanozyme in EC109DDP, EC9706DDP, and TE1DDP cells, the cells were respectively seeded in 96-well plates at a density of 6000 cells per well and cultured overnight for adherence. Then, the cells were treated with CDDP at 160, 80 μM, 40 μM, 20 μM, 10 μM, 5 μM, 2.5 μM, 1.25 μM, and 0 μM, and HCFe nanozyme at 600 μg/m, 450 μg/m, 300 μg/m, 150 μg/m, 100 μg/m, 50 μg/m, 25 μg/m, 10 μg/m, 5 μg/m, and 0 μg/mL for 48 h. Cell viability was determined using a CCK-8 assay. Combination index (CI) values for CDDP and HCFe nanozyme in EC109DDP, EC9706DDP, and TE1DDP cells were calculated. CI values less than 1 indicate a synergistic effect, values equal to 1 represent an additive effect, and values greater than 1 suggest antagonism.

RNA-sequencing analysis

To explore the characteristics of cisplatin-resistant ESCC cells, the EC109 and EC109DDP cells were respectively seeded in 6-well plates at a density of 5×10^5 cells. After the density of cells reached 90%, the cells were collected for RNA-sequencing analysis.

To explore the mechanism of CDDP combined HCFe nanozyme overcame cisplatin resistance in ESCC cells, the EC109DDP cells were seeded in 6-well plates at a density of 2×10^5 cells and cultured overnight for adherence. Then, the cells were treated with PBS, 5 μM CDDP, 75 μg/mL HCFe nanozyme, and 5 μM CDDP + 75 μg/mL HCFe nanozyme for 48 h. Finally, the cells were collected for RNA-sequencing analysis.

Cellular Pt content determination

To compare intracellular CDDP concentrations between CDDP-resistant and parent cells after being treated with CDDP, CDDP-resistant cells (EC109DDP, EC9706DDP, and TE1DDP), and parent cells (EC109, EC9706, and TE1) were seeded in 6-well plates at a density of 5×10^5 cells per well and cultured overnight to allow adherence. Subsequently, the cells were treated with 10 μM CDDP for 5 h. Following treatment, the cells were washed five times with PBS, collected, and counted. The cell pellets were digested in 0.2 mL aqua regia at 115 °C for 30 min. After cooling, the digests were diluted to a fixed volume, and the platinum (Pt) content was quantified using inductively coupled plasma mass spectrometry (ICP-MS).

To investigate CDDP efflux, EC109DDP cells were seeded in 6-well plates at a density of 5×10^5 cells per well and cultured overnight for adherence. The cells were then treated with either 10 μM CDDP alone or 10 μM CDDP combined with 150 μg/mL HCFe nanozyme for 12 h. After incubation, the cells were washed three times with PBS. Half of the EC109DDP cells were harvested to determine the initial intracellular CDDP concentration using ICP-MS. The remaining cells were further incubated in a fresh medium for an additional 12 h. These cells were then washed, harvested, and analyzed to measure the final intracellular CDDP concentration using ICP-MS. The amount of effluxed CDDP was calculated by subtracting the final intracellular CDDP concentration from the initial concentration.

Cellular GSH content detection

To compare the cellular GSH content between CDDP-resistant and parent cells, the CDDP-resistant cells (EC109DDP, EC9706DDP, TE1DDP) and parent cells (EC109, EC9706, and TE1) were seeded in 6-well plates at a density of 5×10^5 cells. After the density of cells reached 90%, the cells were collected and the cellular GSH content was detected by a GSH detection kit.

To examine the depletion of GSH content in EC109DDP cells by CDDP combined HCFe nanozyme, the EC109DDP cells were seeded in 6-well plates at a density of 2×10^5 cells and cultured overnight for adherence. Then, the cells were treated with PBS, 10 μM CDDP, 150 μg/mL HCFe nanozyme, 10 μM CDDP + 150 μg/mL HCFe nanozyme, and 10 μM CDDP + 150 μg/mL HCFe nanozyme + 5 mM NAC for 24 h, and collected for cellular GSH content analysis using a GSH detection Kit.

Western blot assay

To explore the characteristics of cisplatin-resistant ESCC cells, and verify the results of RNA-sequencing, total protein was extracted from cisplatin-resistant cells (EC109DDP, EC9706DDP, and TE1DDP) and parental cells (EC109, EC9706, and TE1), and protein concentrations were measured using a BCA kit. For each sample, 30 μg of protein was separated via sodium dodecyl sulfate-polyacrylamide gel electrophoresis (SDS-PAGE) and transferred onto a 0.22 μm polyvinylidene difluoride (PVDF) membrane. The membranes were incubated overnight at 4 °C with MRP2 antibody (ab187644), Nrf2 antibody (ab62352), GPX4 antibody (ab125066), and β-actin antibody (ABclonal, AC028) After three washes, the membranes were incubated with secondary antibodies at room temperature for 1 h, washed five times, and visualized using enhanced chemiluminescence reagents. The images were obtained using a MiniChemi 610 chemiluminescent imaging system, and analyzed by ImageJ 1.53q software.

To compare the expression levels of DNA damage- and apoptosis-related proteins between CDDP-resistant and parent cells, after being treated with CDDP, the CDDP-resistant cells (EC109DDP, EC9706DDP, and TE1DDP) and parent cells (EC109, EC9706, and TE1), were seeded in 6-well plates at a density of 2×10^5 cells per well and cultured overnight for adherence. The cells were treated with PBS or 20 μM CDDP for 24 h, followed by protein extraction as described above. PVDF membranes containing separated proteins were incubated with γ-H2AX antibody (Abcam, ab81299), Cleaved-caspase 3 antibody (Abcam, ab32042), and β-Actin antibody (ABclonal, AC028). Secondary antibody labeling and chemiluminescence imaging were performed as described.

To analyze the phosphorylated NF-κB, NF-κB, and MRP2 expressions in EC109DDP cells, cells were seeded and cultured for 24 h, followed by treatment with PBS, 10 μM CDDP, 150 μg/mL HCFe nanozyme, 150 μg/mL HCFe nanozyme + 10 μM JSH-23, 150 μg/mL HCFe nanozyme + 5 mM NAC, 10 μM CDDP + 150 μg/mL HCFe nanozyme, 10 μM CDDP + 150 μg/mL HCFe nanozyme + 10 μM JSH-23, and 10 μM CDDP + 150 μg/mL HCFe nanozyme + 5 mM NAC for another 24 h. Proteins were extracted and analyzed as described above. PVDF membranes were incubated with Phospho-NF-κB p65 (Ser536) antibody (CST, 3033), NF-κB P65 antibody (CST, 8242), MRP2 antibody (ab187644), and β-Actin antibody (ABclonal, AC028). Secondary antibody labeling and chemiluminescence imaging were conducted as described.

To analyze the γ-H2AX and Cleaved-caspase 3 expressions in EC109 and EC109DDP cells, cells were seeded and cultured for 24 h and treated with PBS, 10 μM CDDP, 150 μg/mL HCFe nanozyme, 10 μM CDDP + 150 μg/mL HCFe nanozyme, and 10 μM CDDP + 150 μg/mL HCFe nanozyme + 5 mM NAC for another 24 h. Protein extraction, separation, and analysis were performed as described above. PVDF membranes were incubated with γ-H2AX antibody (Abcam, ab81299), Cleaved-caspase 3 antibody (Abcam, ab32042), and β-Actin antibody (ABclonal, AC028), followed by secondary antibody labeling and chemiluminescence imaging.

To analyze the released Cytochrome C in the cytoplasm of EC109DDP cells, treated cells were harvested, and cytoplasm proteins without mitochondria were extracted via a Mitochondrial Extraction Kit. The protein samples were processed as described above. PVDF membranes were incubated with Cytochrome C antibody (ab133504) and β-Actin antibody (ABclonal, AC028), followed by secondary antibody labeling and chemiluminescence imaging.

Apoptosis analysis

CDDP-resistant cells (EC109DDP, EC9706DDP, and TE1DDP) and parent cells (EC109, EC9706, and TE1) were seeded in 6-well plates at a density of 2×10^5 cells per well and cultured overnight to allow adherence. The cells were then treated with PBS or 20 μM CDDP for 48 h. Following treatment, the cells were harvested, washed three times with PBS, resuspended in 100 μL of binding buffer, and stained with 5 μL Annexin V-FITC and 10 μL PI for 15 min at 37 °C, protected from light. Subsequently, 400 μL of pre-cooled binding buffer was added to each sample, and the stained cells were analyzed using flow cytometry (Becton Dickinson Accuri C6). Data analysis was performed using NovoExpress 1.5.6 software.

Cellular ROS assay

Intracellular ROS levels were assessed using flow cytometry with a DCFH-DA probe. Briefly, EC109DDP cells were seeded in 6-well plates at a density of 5×10^5 cells per well and cultured overnight for adherence. The cells were treated with PBS, 10 μM CDDP, 150 μg/mL HCFe nanozyme, a combination of 10 μM CDDP and 150 μg/mL HCFe nanozyme, or a combination of 10 μM CDDP, 150 μg/mL HCFe nanozyme, and 5 mM NAC for 6 h. After treatment, the medium was removed, and the cells were detached and washed three times with PBS. The cells were then incubated with a 10 μM DCFH-DA fluorescence probe for 30 min at 37 °C in the dark. Fluorescence intensity was measured using flow cytometry (Becton Dickinson Accuri C6) with excitation at 488 nm and emission at 530 nm. Data were analyzed using NovoExpress 1.5.6 software.

Mitochondrial membrane potential assay

The loss of mitochondrial membrane potential was evaluated using a laser scanning confocal microscope (Wetzlar, Germany) and a JC-1 assay kit from Beyotime Biotechnology (Shanghai, China). EC109DDP cells were seeded in 6-well plates at a density of 2×10^5 cells per well and cultured overnight for adherence. HCFe nanozymes (150 μg/mL) were added to the wells and incubated for 6 h, 12 h, and 24 h, respectively. Subsequent steps were performed according to the manufacturer's protocol.

Cellular ATP content determination

Cellular ATP content was quantified using an enhanced chemiluminescence assay with a commercial kit from Beyotime Biotechnology (Shanghai, China). Briefly, EC109DDP cells were seeded in 6-well plates at a density of 2×10^5 cells per well and cultured overnight for adherence. The cells were then treated with PBS, 10 μM CDDP, 150 μg/mL HCFe nanozyme, 10 μM CDDP + 150 μg/mL HCFe nanozyme, and 10 μM CDDP + 150 μg/mL HCFe nanozyme + 5 mM NAC for 24 h. Subsequent steps were performed according to the manufacturer's protocol.

In vivo experiments

To establish a subcutaneous CDDP-resistant ESCC tumor model in mice, 5×10^6 EC109DDP cells were subcutaneously implanted into the lower right flank of 6-week-old female BALB/c nude mice. Tumor size was measured using Vernier calipers, and the tumor volume was calculated using the formula: volume = length × width^2/2.

To evaluate the biodistribution of HCFe nanozyme, when the volume of subcutaneous tumors reached approximately 300 mm^3, female BALB/c-nude mice bearing EC109DDP tumors were injected with Free Cy5.5 or Cy5.5-labeled HCFe nanozyme via tail vein. The distribution of Cy5.5 fluorescence was monitored at predetermined time points (0.5 h, 1 h, 2 h, 4 h, 6 h, 8 h, 12 h, 24 h, 36 h, 48 h, 72 h, and 96 h) using an in vivo imaging system (PerkinElmer, Waltham, MA, USA). 96 h post-injection, major organs and tumors were harvested and imaged to evaluate fluorescence distribution.

To evaluate the biosafety of CDDP combined HCFe nanozyme, healthy BALB/c mice (female, 6–7 weeks) were injected with Saline, 2.5 mg/kg CDDP, 5 mg/kg CDDP, 10 mg/kg CDDP, 20 mg/kg HCFe nanozyme, 50 mg/kg HCFe nanozyme, 100 mg/kg HCFe nanozyme, 2.5 mg/kg CDDP + 20 mg/kg HCFe nanozyme, 2.5 mg/kg CDDP + 50 mg/kg HCFe nanozyme, and 2.5 mg/kg CDDP + 100 mg/kg HCFe nanozyme via the tail vein. In the CDDP + HCFe nanozyme groups, the HCFe nanozyme was injected 6 h earlier than CDDP. Body weight

changes were recorded over two weeks. Fourteen days post-injection, blood samples were collected from mice injected with saline, 2.5 mg/kg CDDP, 50 mg/kg HCFe nanozyme, and 2.5 mg/kg CDDP + 50 mg/kg HCFe nanozyme for serum biochemical tests and blood routine tests. Major organs (heart, liver, spleen, lung, and kidney) were harvested and subjected to hematoxylin and eosin (H&E) staining.

To evaluate the in vivo antitumor efficacy, tumor-bearing female BALB/c nude mice with tumor volumes of approximately 50 mm^3 were randomly divided into four groups ($n = 5$ mice in each group) and treated via tail vein injection with saline, 2.5 mg/kg CDDP, 50 mg/kg HCFe nanozyme, or 2.5 mg/kg CDDP + 50 mg/kg HCFe nanozyme. In the CDDP + HCFe nanozyme group, the HCFe nanozyme was injected 6 h earlier than CDDP. Body weight and tumor volume were measured every other day. After euthanasia, tumors were collected for histological analysis, including hematoxylin and eosin (H&E) staining and terminal deoxynucleotidyl transferase dUTP nick-end labeling (TUNEL) staining.

Statistics and reproducibility

The data here were presented as mean ± standard deviation. The statistical analyses were performed using GraphPad Prism 8.0.1 software. Differences between the two groups were analyzed by two-tailed unpaired student's *t*-test. Comparisons among three or more groups were performed using one-way ANOVA or two-way ANOVA. The survival curve of female tumor-bearing mice was analyzed by log-rank Mantel–Cox test. In all cases, statistical significance was considered when $p < 0.05$. In the microscope and western blotting experiments, at least three independent experiments were performed, and representative images were shown.

Reporting summary

Further information on research design is available in the Nature Portfolio Reporting Summary linked to this article.

Data availability

The RNA sequencing data generated in this study have been deposited in the NCBI Sequence Read Archive (SRA) database under accession code PRJNA1177349. This study utilizes publicly accessible data from the Protein Data Bank (PDB) under accession codes: 7ATJ and 5Y6Q. Data supporting the findings of this work are available within the paper and its Supplementary Information files. Source data are provided with this paper. The full image dataset is available from the corresponding author upon request. Source data are provided with this paper.

References

1. Gao, L. et al. Intrinsic peroxidase-like activity of ferromagnetic nanoparticles. *Nat. Nanotechnol.* **2**, 577–583 (2007).
2. Wei, H. & Wang, E. Nanomaterials with enzyme-like characteristics (nanozymes): next-generation artificial enzymes. *Chem. Soc. Rev.* **42**, 6060–6093 (2013).
3. Gao, L.-Z. & Yan, X.-Y. Discovery and current application of nanozyme. *Acta Agron. Sin.* **40**, 892–902 (2013).
4. Gao, L., Fan, K. & Yan, X. Iron oxide nanozyme: a multifunctional enzyme mimetic for biomedical applications. *Theranostics* **7**, 3207–3227 (2017).
5. Liu, L. et al. Manganese dioxide nanozyme for reactive oxygen therapy of bacterial infection and wound healing. *Biomater. Sci.* **9**, 5965–5976 (2021).
6. Wu, R. et al. Oxidase-like ZnCoFe three-atom nanozyme as a colorimetric platform for ascorbic acid sensing. *Anal. Chem.* **94**, 14308–14316 (2022).
7. Jin, X. et al. Zn–Y dual atomic site catalyst featuring metal–metal interactions as a nanozyme with peroxidase-like activity. *J. Mater. Chem. A* **11**, 2326–2333 (2023).
8. Li, H. et al. Peroxidase-like FeCoZn triple-atom catalyst-based electronic tongue for colorimetric discrimination of food preservatives. *Small* **19**, e2207036 (2023).
9. Boruah, P. K. & Das, M. R. Dual responsive magnetic $Fe_{(3)}O_{(4)}$-$TiO_{(2)}$/graphene nanocomposite as an artificial nanozyme for the colorimetric detection and photodegradation of pesticide in an aqueous medium. *J. Hazard Mater.* **385**, 121516 (2020).
10. Han, K. N., Choi, J. S. & Kwon, J. Gold nanozyme-based paper chip for colorimetric detection of mercury ions. *Sci. Rep.* **7**, 2806 (2017).
11. Wang, Q., Wei, H., Zhang, Z., Wang, E. & Dong, S. Nanozyme: an emerging alternative to natural enzyme for biosensing and immunoassay. *TrAC Trends Anal. Chem.* **105**, 218–224 (2018).
12. Meng, Y., Li, W., Pan, X. & Gadd, G. M. Applications of nanozymes in the environment. *Environ. Sci. Nano* **7**, 1305–1318 (2020).
13. Wei, J., Yang, L., Luo, M., Wang, Y. & Li, P. Nanozyme-assisted technique for dual mode detection of organophosphorus pesticide. *Ecotoxicol. Environ. Saf.* **179**, 17–23 (2019).
14. Li, M., Chen, J., Wu, W., Fang, Y. & Dong, S. Oxidase-like MOF-818 nanozyme with high specificity for catalysis of catechol oxidation. *J. Am. Chem. Soc.* **142**, 15569–15574 (2020).
15. Wang, Y. et al. Coordination number regulation of molybdenum single-atom nanozyme peroxidase-like specificity. *Chem* **7**, 436–449 (2021).
16. Xu, G. et al. Electron lock manipulates the catalytic selectivity of nanozyme. *ACS Nano* **18**, 3814–3825 (2024).
17. Xu, B. et al. A bioinspired five-coordinated single-atom iron nanozyme for tumor catalytic therapy. *Adv. Mater.* **34**, e2107088 (2022).
18. Wang, Q., Liu, J., He, L., Liu, S. & Yang, P. Nanozyme: a rising star for cancer therapy. *Nanoscale* **15**, 12455–12463 (2023).
19. Chen, Z. et al. Dual enzyme-like activities of iron oxide nanoparticles and their implication for diminishing cytotoxicity. *ACS Nano* **6**, 4001–4012 (2012).
20. An, Q. et al. Peroxidase-like activity of Fe3O4@carbon nanoparticles enhances ascorbic acid-induced oxidative stress and selective damage to PC-3 prostate cancer cells. *ACS Appl. Mater. Interfaces* **5**, 13248–13257 (2013).
21. Veitch, N. C. Horseradish peroxidase: a modern view of a classic enzyme. *Phytochemistry* **65**, 249–259 (2004).
22. Hakansson, K. O., Brugna, M. & Tasse, L. The three-dimensional structure of catalase from *Enterococcus faecalis*. *Acta Crystallogr D. Biol. Crystallogr* **60**, 1374–1380 (2004).
23. Poulos, T. L. Heme enzyme structure and function. *Chem. Rev.* **114**, 3919–3962 (2014).
24. Liu, Y. & Wang, Z. G. Heme-dependent supramolecular nanocatalysts: a review. *ACS Nano* **17**, 13000–13016 (2023).
25. Orme-Johnson, W. H. Iron–sulfur proteins: structure and function. *Annu. Rev. Biochem.* **42**, 159–204 (1973).
26. Brzóska, K., Meczyńska, S. & Kruszewski, M. Iron–sulfur cluster proteins: electron transfer and beyond. *Acta Biochim. Polonica* **53**, 685–691 (2006).
27. Przybyla-Toscano, J., Christ, L., Keech, O. & Rouhier, N. Iron–sulfur proteins in plant mitochondria: roles and maturation. *J. Exp. Bot.* **72**, 2014–2044 (2021).
28. Bunău, O. & Joly, Y. Self-consistent aspects of x-ray absorption calculations. *J. Phys. Condens. Matter* **21**, 345501 (2009).
29. Wang, B. et al. A general metal ion recognition strategy to mediate dual-atomic-site catalysts. *J. Am. Chem. Soc.* **146**, 24945–24955 (2024).
30. Zhang, R. et al. Edge-site engineering of defective Fe–N(4) nanozymes with boosted catalase-like performance for retinal vasculopathies. *Adv. Mater.* **34**, e2205324 (2022).
31. Wang, Z., Shen, X., Gao, X. & Zhao, Y. Simultaneous enzyme mimicking and chemical reduction mechanisms for nanoceria as a bio-antioxidant: a catalytic model bridging computations and experiments for nanozymes. *Nanoscale* **11**, 13289–13299 (2019).

32. Wang, Z. et al. Accelerated discovery of superoxide-dismutase nanozymes via high-throughput computational screening. *Nat. Commun.* **12**, 6866 (2021).
33. Mitoraj, M. P., Michalak, A. & Ziegler, T. A combined charge and energy decomposition scheme for bond analysis. *J. Chem. Theory Comput.* **5**, 962–975 (2009).
34. Gao, X. J., Zhao, Y. & Gao, X. Catalytic signal transduction theory enabled virtual screening of nanomaterials for medical functions. *Acc. Chem. Res.* **56**, 2366–2377 (2023).
35. Shen, X., Wang, Z., Gao, X. J. & Gao, X. Reaction mechanisms and kinetics of nanozymes: insights from theory and computation. *Adv. Mater.* **36**, e2211151 (2024).
36. Shen, X., Wang, Z., Gao, X. & Zhao, Y. Density functional theory-based method to predict the activities of nanomaterials as peroxidase mimics. *ACS Catal.* **10**, 12657–12665 (2020).
37. Chen, Z., Yu, Y., Gao, Y. & Zhu, Z. Rational design strategies for nanozymes. *ACS Nano* **17**, 13062–13080 (2023).
38. Gao, X. J., Yan, J., Zheng, J. J., Zhong, S. & Gao, X. Clear-box machine learning for virtual screening of 2D nanozymes to target tumor hydrogen peroxide. *Adv. Health. Mater.* **12**, e2202925 (2023).
39. Dagogo-Jack, I. & Shaw, A. T. Tumour heterogeneity and resistance to cancer therapies. *Nat. Rev. Clin. Oncol.* **15**, 81–94 (2018).
40. Galluzzi, L. et al. Molecular mechanisms of cisplatin resistance. *Oncogene* **31**, 1869–1883 (2012).
41. Cheng, M. et al. Advances in the theranostics of oesophageal squamous carcinoma. *Adv. Ther.* **6**, 2200251 (2023).
42. Li, Y., Zhang, X., Wang, Z., Li, B. & Zhu, H. Modulation of redox homeostasis: a strategy to overcome cancer drug resistance. *Front Pharm.* **14**, 1156538 (2023).
43. Mirzaei, S. et al. Elucidating role of reactive oxygen species (ROS) in cisplatin chemotherapy: a focus on molecular pathways and possible therapeutic strategies. *Molecules* **26**, 2382 (2021).
44. Cui, Q. et al. Modulating ROS to overcome multidrug resistance in cancer. *Drug Resist. Updat* **41**, 1–25 (2018).
45. Wang, W. et al. Emodin enhances sensitivity of gallbladder cancer cells to platinum drugs via glutathion depletion and MRP1 downregulation. *Biochem. Pharmacol.* **79**, 1134–1140 (2010).
46. Li, X. et al. Emodin enhances cisplatin-induced cytotoxicity in human bladder cancer cells through ROS elevation and MRP1 downregulation. *BMC Cancer* **16**, 578 (2016).
47. Yamasaki, M. et al. Role of multidrug resistance protein 2 (MRP2) in chemoresistance and clinical outcome in oesophageal squamous cell carcinoma. *Br. J. Cancer* **104**, 707–713 (2011).
48. Makishima, M. et al. Interleukin-18 down-regulates multidrug resistance-associated protein 2 expression through farnesoid X receptor associated with nuclear factor kappa B and Yin Yang 1 in human hepatoma HepG2 cells. *PLoS One* **10**, e0136215 (2015).
49. Arfin, S. et al. Oxidative stress in cancer cell metabolism. *Antioxidants* **10**, 642 (2021).
50. Huang, F. et al. Dual-site biomimetic Cu/Zn-MOF for atopic dermatitis catalytic therapy via suppressing fcgammar-mediated phagocytosis. *J. Am. Chem. Soc.* **146**, 3186–3199 (2024).
51. Lu, X. et al. Bridging oxidase catalysis and oxygen reduction electrocatalysis by model single-atom catalysts. *Natl Sci. Rev.* **9**, nwac022 (2022).
52. Lu, X. et al. Bioinspired copper single-atom catalysts for tumor parallel catalytic therapy. *Adv. Mater.* **32**, e2002246 (2020).
53. Lu, X. et al. Single-atom catalysts-based catalytic ROS clearance for efficient psoriasis treatment and relapse prevention via restoring ESR1. *Nat. Commun.* **14**, 6767 (2023).
54. Ravel, B. & Newville, M. ATHENA, ARTEMIS, HEPHAESTUS: data analysis for X-ray absorption spectroscopy using IFEFFIT. *J. Synchrotron Radiat.* **12**, 537–541 (2005).
55. Zabinsky, S. I., Rehr, J. J., Ankudinov, A., Albers, R. C. & Eller, M. J. Multiple-scattering calculations of x-ray-absorption spectra. *Phys. Rev. B Condens Matter* **52**, 2995–3009 (1995).
56. Frisch M. J. et al. *Gaussian 09, Revision A.02* (Gaussian, Inc. Wallingford, 2016).
57. Becke, A. D. Density-functional thermochemistry. III. The role of exact exchange. *J. Chem. Phys.* **98**, 5648–5652 (1993).
58. Petersson, G. A. & Al-Laham, M. A. A complete basis set model chemistry. II. Open-shell systems and the total energies of the first-row atoms. *J. Chem. Phys.* **94**, 6081–6090 (1991).
59. Andrae, D., Häußermann, U., Dolg, M., Stoll, H. & Preuß, H. Energy-adjustedab initio pseudopotentials for the second and third row transition elements. *Theor. Chim. Acta* **77**, 123–141 (1990).
60. Reed, A. E., Weinstock, R. B. & Weinhold, F. Natural population analysis. *J. Chem. Phys.* **83**, 735–746 (1985).
61. Becke, A. D. Density-functional exchange-energy approximation with correct asymptotic behavior. *Phys. Rev. A* **38**, 3098–3100 (1988).
62. Perdew, J. P. Density-functional approximation for the correlation energy of the inhomogeneous electron gas. *Phys. Rev. B* **33**, 8822–8824 (1986).
63. Perdew, J. P. Erratum: density-functional approximation for the correlation energy of the inhomogeneous electron gas. *Phys. Rev. B* **34**, 7406 (1986).
64. Velde, G. et al. Chemistry with ADF. *J. Comput. Chem.* **22**, 931–967 (2001).

Acknowledgements

This work was financially supported by the National Natural Science Foundation of China (no. 32000996, J.B.), the China Postdoctoral Science Foundation (no. 2020M682358, J.B.), the China Postdoctoral Science Special Foundation (no. 2020TQ0280, J.B.), and the Grant for International Joint Research Project of the Institute of Medical Science, the University of Tokyo (no. extension-2019-K3005, Y.X.).

Author contributions

B.J. conceptualized and designed the project. S.Z., X.G., Y.M., K.S., M.G., and S.M. performed the experiments and analyzed the results. L.Z., Y.Y., W.J., and Z.W. provided suggestions on animal model construction and data analysis. B.J., X.Y., and L.G. supervised the project. B.J., S.Z., and X.G. wrote the manuscript. All authors discussed and commented on the manuscript.

Competing interests

The authors have declared that no competing interest exists.

Additional information

Supplementary information The online version contains supplementary material available at https://doi.org/10.1038/s41467-024-54868-w.

Correspondence and requests for materials should be addressed to Lizeng Gao, Xiyun Yan or Bing Jiang.

Peer review information *Nature Communications* thanks Lawrence Yoon Suk Lee, Xiangyu Lu, and the other, anonymous, reviewer(s) for their contribution to the peer review of this work. A peer review file is available.